CHAPTER 1

Meso-Scale Modeling—The Key to Multi-Scale CFD Simulation

Wei Wang*, Wei Ge, Ning Yang and **Jinghai Li***

Contents

The EMMS Group, State Key Laboratory of Multi-Scale Complex Systems, Institute of Process Engineering, Chinese Academy of Sciences, Beijing 100190, P.R. China
*Corresponding author, Email address: jhli@home.ipe.ac.cn; wangwei@home.ipe.ac.cn

Advances in Chemical Engineering, Volume 40
ISSN 0065-2377, DOI 10.1016/B978-0-12-387036-0.00005-0

Abstract Meso-scale structure is critical to characterize complex systems in chemical engineering. Conventional two-fluid model (TFM) without meso-scale modeling has proved to be inadequate for describing gas–solid flow systems featuring multi-scale heterogeneity. In this review, it is demonstrated that, based on the energy-minimization multi-scale (EMMS) model, the multi-scale computational fluid dynamics (CFD) for gas–solid systems has reasonably accounted the effects of meso-scale structures and hence upgraded both computational efficiency and accuracy significantly. This approach has succeeded in predicting the circulating solids flux, revealing the mechanisms of the choking phenomena and resolving the disputes in transport phenomena of gas-fluidized beds. It has also been applied to a wide range of industrial processes including fluid catalytic cracking (FCC), coal combustion, and so on. In all, the multi-scale CFD with EMMS modeling is intrinsically multi-scaled, free from the requirement of clear scale separation, and it can be expected to be an emerging paradigm for the simulation of multiphase flows and reactors.

1. MESO-SCALE STRUCTURE—A COMMON CHALLENGE FOR CHEMICAL ENGINEERING

Chemical engineering encompasses a broad spectrum of scales with regard to time and space, or briefly, it is multi-scaled. Enumerating from small (fast) to big (slow), this spectrum is highlighted with, for example, molecule, molecular assembly, particle, particle cluster, reactor, and process/plant up to the environment, and may be further grouped into three levels, that is, material, reactor and system, as shown in Figure 1. Each level has its own multi-scale features, in forms of a variety of structures. Obviously, how to characterize these multi-scale structures is a common challenge to all three levels, and hence to the whole domain of chemical engineering. In this article, as a specific example to meet the challenge, we will focus on the multi-scale characterization at the reactor level.

1.1 Multi-scale characteristics of chemical reactors

Understanding of a multiphase chemical reactor involves chemical (catalysis) kinetics, hydrodynamics and heat/mass transfers at scales

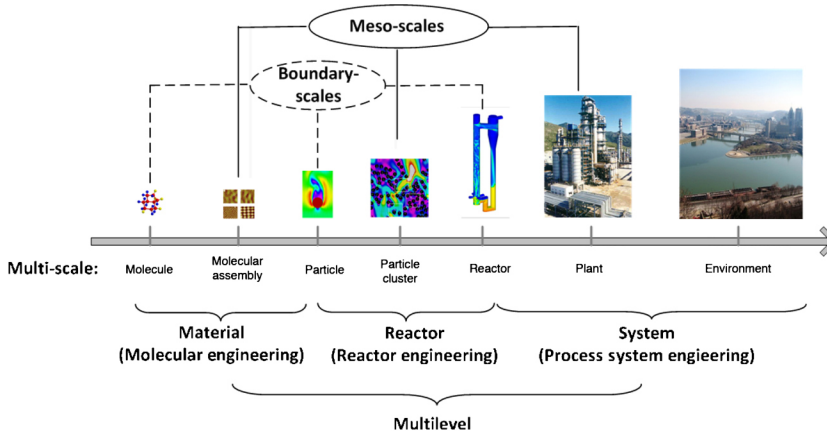

Figure 1 Multi-scale characteristics of chemical engineering and its multilevel classification.
(Adapted from Li **et al**., 2009.)

ranging from molecules to the reactor (Dudukovic, 2009; Li and Kwauk, 2003). Below the (catalyst) particle scale, quantum and molecular dynamics coupled with surface chemistry help us understand the assembly of molecules and (catalysis) reaction mechanism, leading to detailed chemical kinetics. On the scales ranging from catalyst particles and particle clusters, the interactions, within or between fluid vortices and particle aggregates, particle–fluid mixing, as well as heterogeneous heat/mass transfer and reactions, are required to obtain the closure laws for computational fluid dynamics (CFD) modeling. On the reactor scale, global measurement and control can be performed, for optimal operation and design, for which the detailed CFD modeling may shed light on the underlying mechanisms.

The scales involved in such a reactor should be defined in a relative manner. For a chemist, the molecule is at the start and catalyst (particle) at the end of the scales. To reveal the reaction mechanism over a catalyst particle, a sequence of network of ''elementary reactions'' will be needed. Accordingly, on the basis of, for example, the molecular collision theory (Turns, 2000), the ''global reaction'' can be derived in terms of global rate coefficient and reaction order. Here, the resultant reaction mechanism is termed ''global'' by chemists, because the use of it for a specific problem is normally a ''black box'' approach, without knowing exactly the underlying networks or structures of chemical routes from reactants to products. On the other hand, for a chemical reaction engineer, the catalyst (particle) is often the start and the reactor is the end. The reaction free of inner-particle and outer-particle diffusions, that is,

without mass transfer, is normally termed as the ''intrinsic reaction'' (Levenspiel, 1999). On the basis of the ''intrinsic,'' the ''overall'' reaction behavior can be evaluated on the reactor scale by including the effect of flow and mixing within the reactor. In all, a chemist and a chemical engineer may study the same phenomena on certain specific scale (say, the particle scale), but owing to its relative stand, this scale may be viewed as the ''intrinsic'' or the ''global.'' That is the reason why we need to define the scales in a relative manner, namely, the micro-, meso- and macro-scales. The ''micro'' in a field may be the ''macro'' in another field, and vice versa.

1.2 Micro-, meso-, and macro-scales

Normally, the scale with respect to the ''elementary'' or ''intrinsic'' end of one research domain (or level) can be termed the micro-scale, below which the behavior are assumed, or given as input. The scale with respect to the ''global'' end of the research domain can be termed the macro-scale, above which the overall performance can be measured or adjusted. In between, the wide span of scales between the micro- and the macro-scales can be termed the meso-scale, which is characterized by heterogeneous structures with respect to time and space. It is not surprising, then, that the meso-scale is the critical and also the most informative scale to understand the whole range of scales, and it is the bridge between the micro-scale nature and the macro-scale appearance (Li and Ge, 2007). That is also the reason why we do not distinguish the usage between ''structure'' and ''meso-scale structure'' in the following discussions.

Following the above definition of scales, we can see, for a fluidized bed reactor, the single particle stands for the micro-scale, on which the fluid–particle interactions have been thoroughly investigated and summarized into well-accepted laws, for example, the standard drag coefficient for momentum transfer, the Ranz relation for heat/mass transfer (Ranz, 1952), and so on. To the opposite end, the reactor represents the macro-scale, over which we may measure and control the temperature, pressure, and gas flow rate, to achieve optimal conversion of products with as least as possible power consumption and pollutant emissions. In between, the meso-scale is characterized with a variety of heterogeneous structures such as bubbles or clusters, and so on, to which the mirco-scale particles react nonlinearly. Within the meso-scale structures, the behavior of individual particles is quite different from that of isolated, single particles, with local asymmetry and accelerations that may result in additional factors that cannot be accounted for by simple averaging of single-particle behaviors. That is right the reason why we need the scale-up of a reactor. To some extent, the scale-up is to grasp

the effects of the meso-scale structures. To this end, in-depth understanding of the meso-scale structure is critical.

1.3 Meso-scale structure—spatiotemporal features

The meso-scale structure is likely dynamic and hereby hard to characterize. By comparison, for static structure, as is the case in a fixed bed, though there is a wide variety of morphology for the packed state, it is still possible to enumerate its variation and then analyze its statistical effects through subparticle level simulations (Dixon *et al*., 2006; Van der Hoef *et al*., 2006) or experiments (Ergun, 1952; Ranz, 1952). The micro-scale difference of static structures can be smoothed up with increase of samples, and then the structural effects are comparatively easier to grasp. For dynamic structure, however, as is the case in a fluidized bed, the degrees of freedom increases significantly with continuous evolution of shapeless bubbles/clusters (Kunii and Levenspiel, 1991), and then, it is hard to statistically analyze the structural effects by enumerating samples.

1.3.1 Time-averaged characterization

To characterize the meso-scale structure from a series of fluctuating/random signals, the mean (or expectation) values in terms of time averaging or probability-weighted averaging are mostly used. On the basis of that, the fluctuation, the variance or its square root, the standard deviation, and higher order moments can be derived (Pope, 2000). For a fluidized bed, for instance, it was reported that there exists a bimodal probability distribution over the entire range of solids fraction, one apex corresponding to the dense ''cluster'' phase and the other to the dilute ''broth'' phase (Li and Kwauk, 1994), respectively. Lin *et al*. (2001) found that the dense phase (clusters) has a Gaussian solids fraction distribution and the dilute phase (broth or void) has a log-normal solids fraction distribution, and they recommended that the mean solids fraction of the cluster minus three times its standard deviation as the criterion to distinguish clusters from the broth. Another approach to identify a cluster is to set the time-averaged solids fraction plus n-times its standard deviation as the threshold value for clusters. However, how to define the value of n over the fluctuating signals remains an art rather than a science. For example, Soong *et al*. (1994) and Liu *et al*. (2005) suggested $n = 3.0$, Sharma *et al*. (2000) suggested $n = 2.0$, while Manyele *et al*. (2002) suggested $n = 1.0$–1.4 according to their respective sensitivity analysis. Besides this uncertainty in definitions, measurement ambiguity owing to different configuration of probes will also lead to different descriptions of structures, as recognized by Reh and

Li (1991). All of these, however, suggest that reducing the meso-scale structures into two-phase description is a reasonable simplification.

Following the above two-phase description, we can further define the velocities with respect to the dense ''clusters'' and dilute ''broth.'' The slip velocity in dense clusters is normally much lower than that in the dilute ''broth,'' which results in dense clusters falling down along the wall while upflowing gas in broth tearing off particles out of the clusters (Li *et al*., 1993). Seeing from the micro-scale using direct numerical simulations (DNS) approaches, Ma *et al*. (2006) simulated a periodic suspension of 1024 solid particles and found that heterogeneity is observable even in such tiny system in forms of particle clusters, formed progressively from uniform suspension. This was demonstrated to be results of the compromise between the tendency of the solids to maintain low gravitational potential and that of the gas phase to maintain low energy consumption for suspending and transport when flowing through the solids. According to the heterogeneity index proposed in that work, a characteristic scale can be determined where the heterogeneity is most evident. The heterogeneity is also found in the velocity of the solids. Although Gaussian distribution is still valid for the velocity component in each direction, the variance in the gravitational (vertical) direction is notably higher than in the horizontal direction. That is, the velocity distribution is anisotropic. Equal partitioning of the particle kinetic energy, as in the case of gas molecules, is not reached. The same thing happens to the drag force distribution. The distributions of the drag force components are Gaussian or nearly Gaussian, but the solids in the dilute phase suffer far larger drag forces than those in the center of the dense phase. These are all clear evidence that the solid phase is in non-equilibrium state, which must be taken into account in CFB simulations.

The same mean velocity of clusters may have different moving tendency. If the net force exerted on a cluster is positive against gravity, its solids fraction decreases and the cluster diffuses or fragments; if the net force is negative, the cluster is forming or concentrating (Liu *et al*., 2005). Such an imbalance between the dense and dilute phases requires more degrees of freedom to account for the dynamic factors.

1.3.2 Dynamic characterization

The acceleration is a direct measure to the dynamic factors. However, there are few reports, if not to say none, about that for meso-scale structures. In a recent attempt, Meng *et al*. (2009) made use of the multiple sensors of an X-ray computerized tomography (CT) to measure the cluster accelerations. Instead of the conventional use of CT for cross-sectionally scanning the solids distribution, they erected the X-ray fan-beam and the sensors to follow the vertical movement of clusters

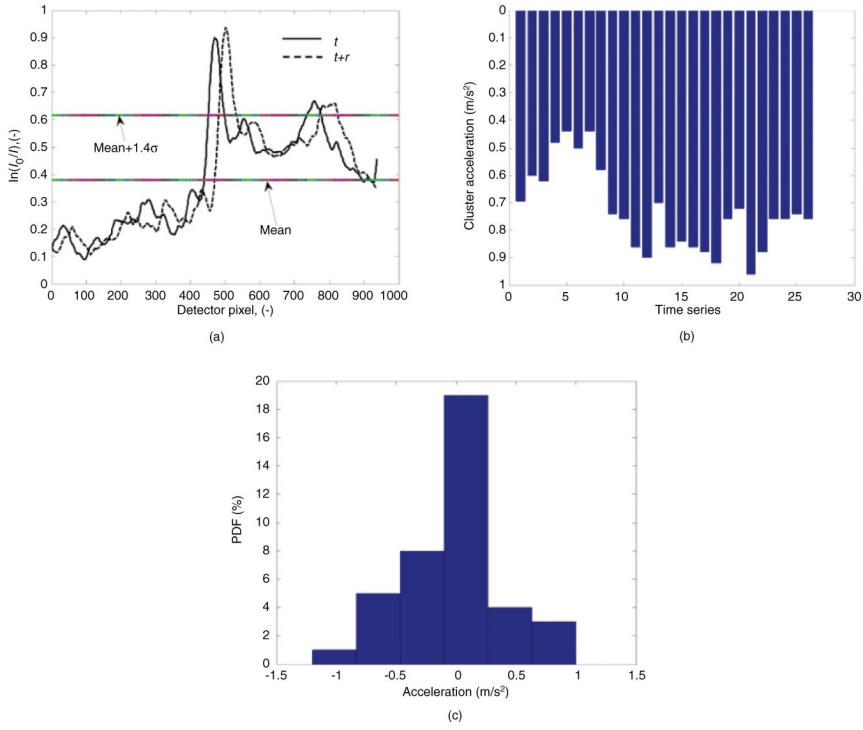

Figure 2 X-ray measurement of cluster acceleration (Meng *et al*., 2009). (a) Identification of cluster with mean + 1.4σ on two correlated series of X-ray signals at time t and $t + \tau$; (b) the cluster velocity series calculated by dividing the displacement with time step; (c) the probability density function of cluster acceleration. (Air-glass beads, $U_g = 3.57$ m/s, $G_s = 65.13$ kg/(m^2 s), X-ray measurement platform was 1 m above the secondary distributors of a 10.5 m high CFB riser.)

along the riser wall of a CFB. As shown in Figure 2, by cross-correlation analysis of a time series of the detected signals of solids fraction of clusters (Figure 2a), the cluster velocity series can be determined by dividing the displacement with the time step (Figure 2b), and likewise, the cluster accelerations can be calculated by dividing the cluster velocity with the time step (Figure 2c). It was found that the clusters near the wall are under force balance in average, in the sense that the measured accelerations are in normal distribution with mean value of about zero. The nonzero accelerations closely relate to the deforming, aggregating and fragmenting of clusters, and this is the basic difference between a dynamic cluster and a moving porous medium. More experiments are under way and can be expected to help grasp the dynamic nature of the meso-scale clusters.

Besides the time-averaged and the dynamic characterizations, the correlations between different scales add more complexities to the meso-scale structure. For example, the intensive exchange between meso-scale clusters and dispersed particles will reduce the cross-correlation coefficient and then make it hard to discern a cluster from broth. Such complexity requires more efforts in exploring the dominant mechanisms underlying the correlations, which will be discussed and exemplified by multi-scale CFD in later sections.

1.4 Critical effect of meso-scale structure

The meso-scale structure is a common challenge for chemical engineering, owing not only to its difficulty to grasp but also to its critical effects on the flow, heat/mass transfer, and reaction behavior. For a gas-fluidized bed, for example, the single-particle behavior has been thoroughly investigated. There are common senses as to the interphase momentum or heat/mass transfer, and so on (Crowe, 2006). When the meso-scale structure is involved, however, great disputes ensue even on how to define the drag force and the added mass force at those scales; the relative importance of these different forces (say, the drag force and the added mass force) may be reversed (De Wilde, 2005), and the resultant variation may be up to several orders of magnitude (Li and Kwauk, 2001; Wang *et al.*, 2010b). Normally, these interphase forces play the decisive role in affecting the reactor behavior. Therefore, how to quantify these forces, especially the drag force for fluidized beds, is of overwhelming importance (Agrawal *et al.*, 2001; Li and Kwauk, 1994, 2001).

Figure 3 schematically shows the striking difference in literature, on flow, mass transfer and reactions in terms of drag coefficient, Sherwood number and reaction rate coefficient, respectively. For gas–solids riser flow, different drag coefficients may cause variance up to three orders of magnitude. Their general trends with increasing solids concentration are also different. For mass transfer in a CFB, even higher difference up to five orders of magnitude has been reported (Breault, 2006). For the reaction rate of, for example, char combustion, the reported values differ greatly by also several orders of magnitude due to the complex properties and structures of char (Basu and Fraser, 1991; Nikss *et al.*, 2003), while it is hard to quantify such differences and no general correlation is available. How to explain and quantify these structure-induced differences in flow, transfers and reaction remain challenges and also critical questions to chemical engineering research. In what follows we will try to tackle these challenging issues with our tentative answers by introducing multi-scale CFD approach.

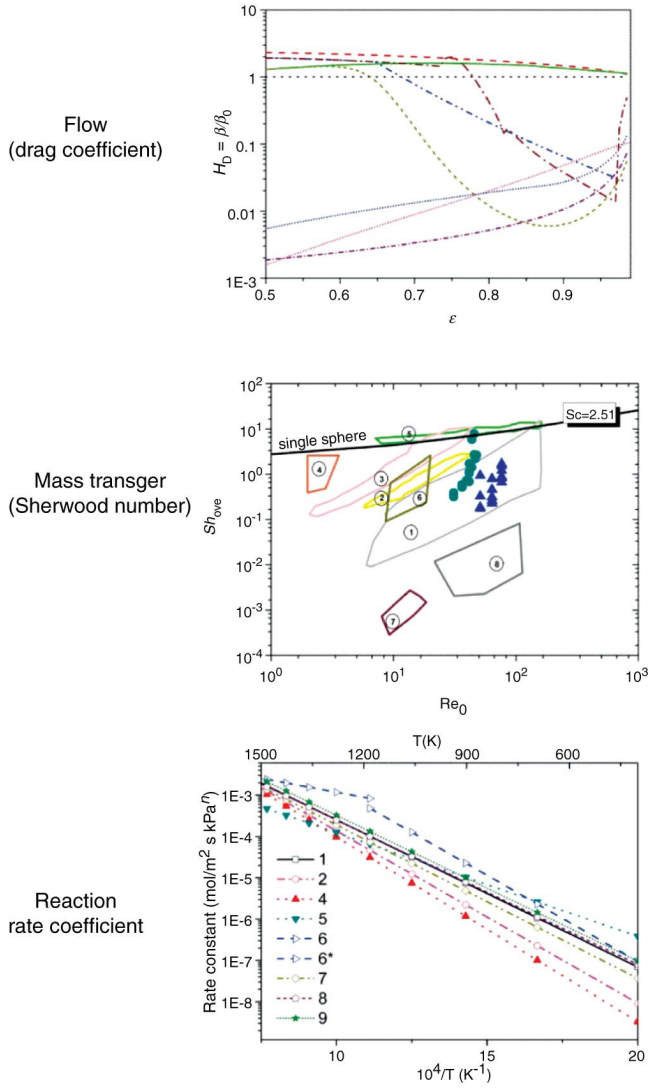

Figure 3 Literature discrepancies in drag coefficient, in mass transfer for CFB due to meso-scale structures and in char reaction rate coefficient. For the drag coefficients, curves are adapted from Wang *et al*. (2010); for the mass transfer, curves are adapted from Dong *et al*. (2008a); for the coal reaction, different symbols refer to different coal data.

2. MULTI-SCALE CFD—SOLUTIONS FOR HIGH PREDICTABILITY AND SCALABILITY

To capture the meso-scale structure and/or to predict its effects, various modeling approaches have been proposed. The spatiotemporal resolution of these approaches grows with the development of the computer capacity, including the single-scale approaches, direct numerical simulations, and multi-scale approaches.

2.1 Single-scale approach—its limitation on predictability

The simplest approach is the classic chemical engineering models which include, for example, the plug flow model, the continuously stirred tank reactor (CSTR) model and their hybrid models (Levenspiel, 1999), and so on. The plug-flow model is a typical single-scale approach, in which the multi-scale flow is reduced into a pipe flow with a characteristic velocity and time scale, every flow elements passing through the pipe uniformly without any structure. Such a model is an extreme simplification to the real flow. To approximate the real flow, one may assemble a series of plug flow models and CSTR models in various networking topologies to fit the overall output in terms of the residence time distribution (RTD). However, such agreement cannot be counted on too much as the classic chemical engineering model in itself is a black box without spatial resolution of what happens inside and beneath.

2.2 Direct numerical simulations—its limitation on scalability

Computational fluid dynamics enables us to investigate the time-dependent behavior of what happens inside a reactor with spatial resolution from the micro to the reactor scale. That is to say, CFD in itself allows a multi-scale description of chemical reactors. To this end, for single-phase flow, the space resolution of the CFD model should go down to the scales of the smallest dissipative eddies (Kolmogorov scales) (Pope, 2000), which is inversely proportional to $Re^{-3/4}$ and of the orders of magnitude of microns to millimeters for typical reactors. On such scales, the Navier–Stokes (NS) equations can be expected to apply directly to predict the hydrodynamics of well-defined system, resolving all the meso-scale structures. That is the merit of the so-called DNS.

For multiphase flow that is normally encountered in fluidized bed reactors, there are two kinds of definitions of the micro-scale: first, it is the scale with respect to the smaller one between Kolmogorov eddies and particles; second, it is the scale with respect to the smallest space required for two-phase continuum. If the first definition is adopted, the

space resolution of the governing equations should be smaller than the microlength scale, where the governing equations may have a variety of choices, including NS equations, lattice Boltzmann method (LBM) (Wolf-Gladrow, 2000), and smoothed particle hydrodynamics (SPH) (Monaghan, 2005) and particle motion may be described by, for example, discrete element method or discrete particle method. In this way, each particle can be tracked individually with the fluid–particle interactions described in classic Newton mechanics and the particle–particle interaction with, for example, rigid body mechanics. Here the parameters such as the fluid viscosity, restitution coefficient and the elasticity modulus are needed as input from lower scale theory or experimental measurements. For example, the kinetic theory of gas can be applied to determine the gas phase viscosity for DNS.

If the second definition is adopted instead, as is the case of two-fluid model (TFM), the so-called fine-grid TFM will take the place of DNS, by which the subgrid closure relations may be obtained for the coarse-grid TFM simulation. That is, coarse-grid TFM will behave as the large eddy simulations (LES) or Reynolds-averaged Navier–Stokes (RANS) for two-phase flows. Obviously, the critical issue of this kind of DNS heavily relies on the accuracy of the basic governing equations for the continua. It should be noted, the terms of ''fine-grid'' and the ''coarse-grid'' that will appear repeatedly in this article are defined in a relative manner, as follows: the ''fine-grid'' means that the grid is smaller than the micro-scale and there is no need of subgrid modeling anymore, while the ''coarse-grid'' means that the grid is larger than the micro-scale; there are subgrid structures and subgrid modeling must be included to guarantee the accuracy.

It has been widely recognized that the computational demand of any type of the above DNS is tremendous. In the literature, DNS of gas–solid suspension was performed over a domain that is comparable in size with a computational cell and only thousands of particles are tracked. That scale is far less than that involved in industrial reactors, which is normally of the order of meters, with amount of particles (e.g., FCC particle, 10–100 m) in the range of 10^{12}–10^{15}. As to temporal evolution, the time step of the gas–solid DNS simulations is limited by both the Kolmogorov time scale that is inversely proportional to $\mathrm{Re}^{-1/2}$ and the particle collision time scale. The typical time step was reported less than microseconds (Ma *et al*., 2006) and the simulated physical time can hardly reach the order of magnitude for real processes that may be in minutes or hours. Though recent progress in GPU-based technology harnesses the speedup of parallel computing by one to two orders of magnitude (Chen *et al*., 2009; Xiong *et al*., 2010), it is still formidable, at least in foreseeable future, to apply DNS to predict hydrodynamics of a reactor.

2.3 Multi-scale CFD approach—a compromise of predictability and scalability

To meet the industrial demand for both large-scale computation and good predictability, the reasonable way out is not to simulate from the beginning of the micro-scale, but to use coarse-grid simulation with meso-scale modeling for the effects of structure. This kind of approach can be termed the ''multi-scale CFD.'' It is entitled ''multi-scale,'' not because the problem it solves is multi-scale, but because its meso-scale model contains multi-scale structure parameters.

According to the choice of meso-scale models, we may divide the multi-scale CFD into two branches: the ''correlative'' and the ''variational,'' as named in Li and Kwauk (2003) and will be discussed in the following sections.

2.3.1 Correlative

The ''correlative'' multi-scale CFD, here, refers to CFD with meso-scale models derived from DNS, which is the way that we normally follow when modeling turbulent single-phase flows. That is, to start from the Navier–Stokes equations and perform DNS to provide the closure relations of eddy viscosity for LES, and thereon, to obtain the larger scale stress for RANS simulations (Pope, 2000). There are a lot of reports about this correlative multi-scale CFD for single-phase turbulent flows. Normally, clear scale separation should first be distinguished for the correlative approach, since the finer scale simulation need clear specification of its boundary. In this regard, the correlative multi-scale CFD may be viewed as a ''multilevel'' approach, in the sense that each span of modeled scales is at comparatively independent level and the finer level output is interlinked with the coarser level input in succession.

Following the same methodology, one may start from the basic governing equations for gas–solid two-phase flows and performs in sequence the DNS, LES, and RANS for fluidization simulations. As discussed above, depending on the space resolution of different DNS approaches, one can further find two paradigms for that practice. The first may be referred to Agrawal *et al*. (2001) and Igci *et al*. (2008), where the effective drag coefficients for coarse-grid simulation were derived from the fine-grid TFM simulation results over periodic domains. Another paradigm starts from subparticle simulations; the effective drag coefficient can be then obtained from lattice Boltzmann simulations of gas flow through a fixed bed of particles (Van der Hoef *et al*., 2006) or SPH simulations of a gas–solid suspension (Ma *et al*., 2006).

These subparticle simulations also allow in-depth understanding of the applicability of their closure laws for higher scale simulations. For example, Ma *et al*. (2009) found that the typical ''drafting–kissing–

tumbling'' process describing the instability of sedimentation of few particles remains effective in shaping the heterogeneity in gas–solid systems, but it was repeated on groups of particles rather than individual particles, which eventually leads to the formation of clusters, the typical meso-scale structure in gas–solid suspensions. It is interesting to note that, for the whole suspension, the balance between particle gravity and the drag force on the particles are established almost immediately during this process, and vary very little thereafter, though individual particles may experience acceleration and deceleration constantly. However, the slip velocity between the gas and solid phases increases in a fluctuating manner for a much longer time before reaching a statistically plateau value, this is driven by, or in other words, reflected by, the structural changes in the destabilizing process. Clustering has apparently reduced the intensity of interphase friction, which, according to the EMMS model, is both favorable for the solid particles to reach minimum local voidage and the gas phase to produce least dissipation. Xiong *et al*. (2010) found more distinct heterogeneous structures in gas–solid suspensions with more solid particles. With the help of massive parallel computation and recently by GPU computing, they were able to simulate an area up to several square centimeters, laden with 75-m spherical solid particles at a volume concentration of about 15%, and the gas–solid density ratio above 1000. A preliminary study on the scale-dependence of the heterogeneity was then possible. As shown in Figure 4, they simulated up to 30,240 solid particles, and found that local fluctuations, in both particle velocity and drag force, increase with the size of the simulated domain, whereas the overall temporal fluctuation of these quantities is still ablating with the increase of domain size, which means the heterogeneity is indeed more significant in larger systems. However, an asymptotic scale-dependence is evident in different quantities, such as the steady-state average slip velocity, as wells as its fluctuation in time. That is, the rates of increase slow down gradually as the domain size increase, and finally a plateau of these quantities are reached. It is also in agreement with earlier studies using TFMs (Agrawal *et al*., 2001; Ge *et al*., 2008; Wang, 2008) and theoretical projection of the EMMS model. Together with the mesh-dependence, these findings validate the use of (nearly) scale-independent models for describing the properties of the heterogeneity on meso-scale, such as the drag law and solid-phase stress law, at least in a certain range of scales.

Following the above approach, the correlative multi-scale CFD reduces the computation cost by transforming information over a range of scales into meso-scale models. With these works, it seems feasible to establish a numerical experiment facility to consider thoroughly the

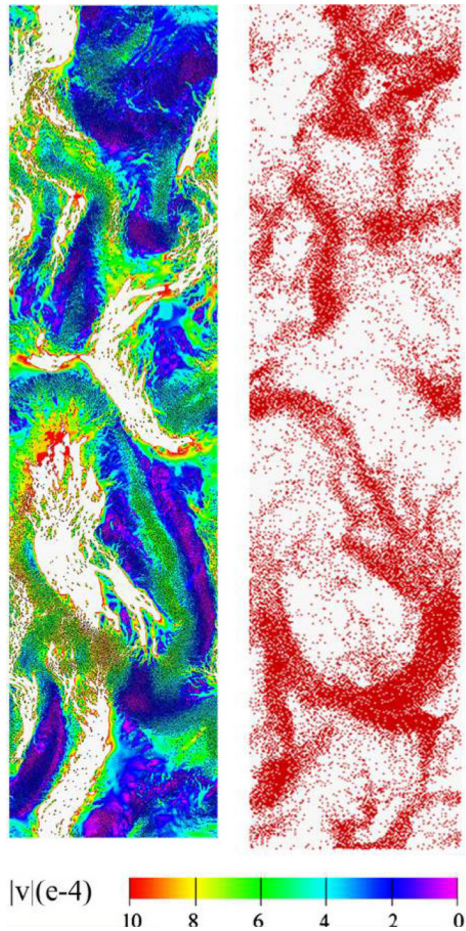

Figure 4 Snapshot from a dynamic DNS simulation of two-dimensional gas–solid system with 30,240 solid particles (Xiong *et al*., 2010). (The right figure shows the distribution of solid particles and to the left the gas velocity field is added; $|v|$ in color spectrum denotes the gas velocity magnitude.)

meso-scale effects of gas–solid systems, which is otherwise a formidable task for both theoretical studies and experimental measurements. We may expect that further development of DNS methods for gas–solid system and the high performance computing technologies will allow new breakthrough to realize it in future (Chen *et al*., 2009). On the other hand, however, severe challenges have to be solved first to meet this forthcoming possibility.

The first challenge lies in how to sufficiently sweep all the possible states of flow structures over the wide range of scales. As discussed

above, the meso-scale structure is characterized with dynamic variation. Its effects are related inherently with accelerations and random evolution of structures. The normal practice by accounting for these effects with void fraction has proved to be insufficient (Wang *et al*., 2010b). Therefore, how to introduce new variables for the dynamic structure will be a challenge to both modeling and computation.

Another challenge to the correlative multi-scale CFD is how to incorporate the macro-scale influence into the meso-scale modeling. It is well known that there could be backscatter contributions for the transfer of energy in turbulent flows (Pope, 2000). In a fluidized bed, there are also evidence that the meso-scale clusters are affected by both the macro-scale operating conditions and the micro-scale interstitial flows around particles (Grace, 1996; Harris *et al*., 2002; Wang and Li, 2007). However, the normal practice by performing a finer scale simulation over a small periodic domain or a static bed of particles is only related with micro-scale constraint. So, it will be a challenge for correlative methods as to how to introduce macro-scale effects such as the geometric limitation and operating conditions of a reactor. Such a challenge in itself reflects the bilateral coupling/bridging difficulties in meso-scale modeling for most of the multi-scale problems. Certain trans-scale criterion might be needed, or, at least helpful, to untangle this challenge in correlative methods, and this is right to the point that the variational methods will focus on.

2.3.2 Variational

The ''variational'' type of multi-scale CFD, here, refers to CFD with meso-scale models featuring variational stability conditions. This approach can be exemplified by the coupling of the EMMS model (Li and Kwauk, 1994) and TFM, where the EMMS/matrix model (Wang and Li, 2007) at the subgrid level is applied to calculate a structure-dependent drag force.

The variational stability condition describes the ''compromise'' among various dominant mechanisms. In mathematics, the ''compromise'' can be expressed as a multiobjective optimization (Li and Kwauk, 2003). Not like the ''correlative'' multi-scale CFD where separate ranges of scales can be distinguished over which the finer supplies for the coarser, the ''variational'' obtains correlations through the ''compromise'' among the dominant mechanisms that are coupled over the investigated range of scales. As a consequence, the scale separation is not a necessary condition to the ''variational.'' In this regard, the ''variational'' multi-scale CFD is inherently multi-scaled.

More details about the variational type of multi-scale CFD will be addressed in following sections. As to the major challenges it confronts, the first lies in how to distinguish the dominant mechanisms over such

broad range of scales for different systems. For a thermodynamic equilibrium system, we know that the maximum entropy criterion determines its final state; for linear nonequilibrium systems, minimum entropy production rate governs their behavior (Prigogine, 1967); while for the nonlinear nonequilibrium system that is widely encountered in chemical engineering, no single, universal criterion has been discovered yet (Gage *et al*., 1966). That implies we have to search specific stability conditions for different systems (Li and Kwauk, 2003). Recent work has found some clues to establish a general strategy to distinguish the ''dominant mechanisms'' by analyzing the ''compromise'' between them (Li and Kwauk, 2003; Li *et al*., 2004). This strategy has been extended to six other systems besides the gas–solid fluidization, covering single-phase flow, gas–liquid flow, granular flow and emulsions, and so on. More efforts are needed to generalize this strategy for wider range of applications (Ge *et al*., 2007).

Another challenge to the ''variational'' multi-scale CFD lies in the computing scheme, in the sense that the ''dominant mechanisms'' as well as their ''compromise'' in terms of certain stability conditions may relate with scales different from those of CFD computation. A clear example for that situation can be found in gas–solid fluidization (Li *et al*., 2004; Zhang *et al*., 2005), where locally the two dominant mechanisms for particles ($\varepsilon = \min$) and gas ($W_{st} = \min$) can be realized alternately with respect to time and space, with the term for characterizing stability condition fluctuating intensively, while their compromise leads to the stability condition ($N_{st} = \min$) at the meso-scale. When CFD computation is performed at a scale smaller than that, how to incorporate the larger scale stability condition into the CFD description of hydrodynamics will be a hard topic.

In all, there are different approaches for realizing multi-scale CFD, each with distinctive characteristics. Table 1 summarizes the characteristics and the challenges of these two kinds of multi-scale CFD approaches. To manifest their respective utilization and features, in what follows we will compare them with examples on gas-fluidized bed simulations.

2.3.3 Applications of the multi-scale CFD

Limited to computing capability, the following analysis confines the DNS to the fine-grid TFM simulation, which offers meso-scale closures for the correlative, coarse-grid TFM simulations. For comparison, the variational type of multi-scale CFD takes the EMMS-based models to close TFM simulations.

2.3.3.1 Periodic domain simulations. As to the fine-grid TFM, we followed the scheme proposed by Agrawal *et al*. (2001) and first performed simulations over periodic 2D domains, whose

Table 1 Comparison between the correlative and the variational types of multi-scale CFD

	Correlative (e.g., closure for TFM with DNS results)	Variational (e.g., coupling between EMMS and TFM)
Characteristics	• Clear scale separation is necessary (multileveled)	• Clear scale separation is not necessary (intrinsically multi-scaled)
	• Computationally expensive	• Computationally saving
Challenges	• Exhaustive search of all states of dynamic structures	• Determination of dominant mechanisms and stability conditions
	• Incorporation of macro-scale influence into meso-scale modeling	• Trans-scale coupling scheme between CFD and meso-scale models

dimensionless size maintains the same value of 200×800 (scaled with the particle diameter), which is comparable in physical size with a grid in coarse-grid simulations for fine particles of Geldart group A. The domain was meshed with uniform, square grids and refined gradually to investigate the effect of grid size. The commercial software Fluent® 6.2.16 was used as the solver of TFM. The solid stress and drag coefficient terms therein need to be closed. For simplicity, the algebraic form of the granular temperature equation derived from the kinetic theory of granular flow (KTGF) (Gidaspow, 1994) was taken to close the solids pressure and solids viscosity, and so on. The correlative CFD adopts the hybrid drag coefficient combining Wen and Yu's and Ergun's relations (Gidaspow, 1994) (for brevity, Model G), which has been widely accepted as the standard relation, while the variational CFD adopts the EMMS-based subgrid model, that is, EMMS/matrix (Lu *et al.*, 2009; Wang and Li, 2007) (for brevity, Model M). Model G was obtained from homogeneous fluidization and packed bed systems, so it may be taken as an extreme example without considering subgrid structures. Model M depends on the structure that is resolved by EMMS. To account for the effects of physical properties of the materials used, three types of particles that belong to groups A, B, and D of Geldart classification (Geldart, 1973), respectively, are compared as shown in Table 2 (Lu *et al.*, 2011). At the start of simulations, particles of all cases were uniformly distributed with an identical solids volume fraction of 5%. The periodic boundaries were prescribed in both directions to keep constant solids concentration and the gravity of

Table 2 Physical properties of the fluidized systems simulated

	Group A	Group B	Group D
Particle diameter d_p, m	75	300	1,020
Particle density ρ_p, kg/m^3	1,500	2,500	4,000
Gas density ρ_g, kg/m^3	1.3	1.225	1.225
Gas viscosity $_g$, Pa s	1.8×10^{-5}		
Terminal settling velocity u_T, m/s	0.2184	2.18	8.3
Archimedes number Ar	24.9	2,499.8	157,233.3

particles was balanced by the imposed pressure drop along the vertical direction. The drag force exerted on particles relates with the effective gravity by $\beta = \varepsilon_g(1-\varepsilon_g)(\rho_p - \rho_g)g/u_s$, so that the slip velocity is inversely proportional to the drag coefficient. More details about the settings should be referred to Lu *et al*. (2009, 2011).

For a given periodic domain (or a coarse-grid), the two-phase flow will reach its quasi-steady state with slip velocity fluctuating around its time-average value after a period of time. Figure 5 shows the variation of this time-average, dimensionless slip velocity against grid size for Geldart group A particles. Snapshots of the solids distribution are inset to manifest the meso-scale clusters at corresponding grid resolutions. For the Model G, as shown in Figure 5a, the predicted slip velocity increases with grid refining and finally approaches an asymptote when the grid is thinning to the size as small as several particle diameters.

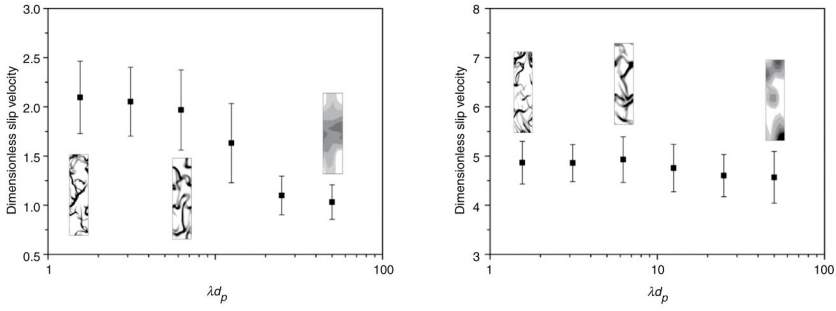

(a) Wen and Yu/Ergun drag coefficient (b) EMMS/matrix drag coefficient

Figure 5 Effect of grid resolution (λ) on the time-averaged dimensionless slip velocity (u_s/u_T). Geldart group A particles are used. The ordinate is scaled with the terminal velocity of single particles ($u_T \approx 21.84$ cm/s) and the abscissa is scaled with the particle diameter d_p. The domain size is 1.5×6 cm^2, comparable to the coarse-grid used in normal simulations.
(After Wang **et al**., 2010b.)

During this refining process, the slip velocity roughly doubles, and accordingly, the effective drag coefficient reduces by 50%. This result coincides with the findings of Agrawal *et al*. (2001). The asymptotic slip velocity implies that there is a threshold for the micro-scale, below which the DNS of TFM can be used to predict the subgrid drag coefficient for coarse-grid simulations. It is interesting to note that, when using Model M, over the investigated range of λ/d_p from about 1 to 100, the solution only weakly depends on the grid size (or even grid independent), as shown in Figure 5b.

Figure 6 gives more comparison for coarser particles. For Geldart group B particles, the slip velocity predicted by the Model G only depends weakly on the grid size, and its value is close to unity. This phenomenon is obviously different from what is observed for Geldart A particles. When the Model M is employed, there exists a similar trend, but with different values. The slip velocity predicted by using Model M is about two times that by using Model G. This difference should be attributed to the subgrid meso-scale modeling in the EMMS/matrix model. For Geldart group D particles, again, results of both models remain almost grid independent, and both of their predicted slip velocities are smaller, and much closer to unity. This gradual reduction of the dimensionless slip velocity reflects the decaying effect of meso-scale structures with increase of particle diameter (or Ar). By comparison, Jin *et al*. (2010) pointed out that, in isotropic turbulent flow laden with heavy particles, with increase of Stokes number ($St > 1$), particles respond to the eddies with larger time scales relative to the Kolmogorov eddies, and then, the level of accumulation drops and

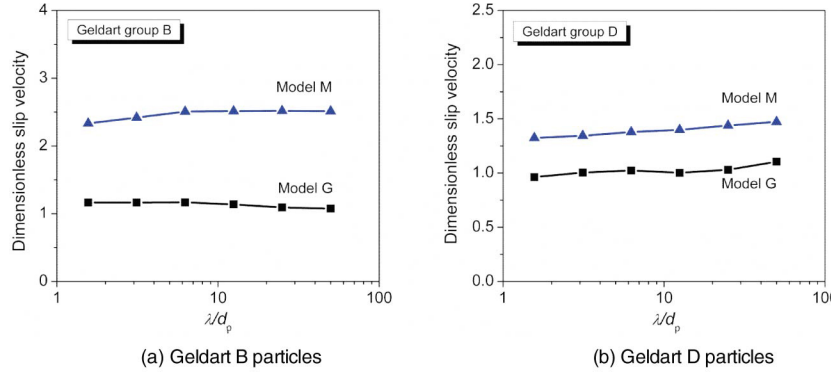

Figure 6 Effect of the periodic domain size on the time-averaged dimensionless slip velocity (u_s/u_T).

particles are more uniformly distributed. More efforts are needed to clarify the relevant mechanisms.

Besides the obvious value difference mentioned above, it is also natural to question why these two drag models cause such different trends. The answer is that there is substantial difference between using the Model G and the Model M. For Model G, the simulations with grid size larger than the threshold value, for example, $\lambda/d_p > 10$ for FCC particles in Figure 5, are coarse-grid without consideration of structures, and hence inadequate for providing the subgrid closure. For Model M, however, the model in itself contains subgrid structure modeling. That is, across the investigated range of grid size, all the simulations can be viewed as ''coarse-grid'' with subgrid meso-scale modeling. If Model M accurately captures the grid-size dependency of the structure (i.e., the core for a subgrid meso-scale model), all these simulations should predict the same, accurate drag closure, for the larger domain, irrespective of what grid resolution they are using. Therefore, the Model M seems satisfying this premise for accuracy, and hence predicts almost the same value of slip velocity, showing a grid-independent trend.

As we know, the structure effect varies with domain size—the effective drag coefficient will decrease with increase of domain size before reaching a plateau of slip velocity (Agrawal *et al*., 2001; Wang, 2008). Therefore, an appropriate meso-scale model should take into account the domain size (or filter size in Andrews *et al*., 2005), either explicitly or implicitly. The typical LES model takes into account this effect by a length scale that selects the minimum resolved eddy size, Δ, explicitly (Ferziger, 1993). In Model M (EMMS/matrix), the grid size is not presented explicitly. However, in its second step, as will be detailed in following sections, the slip velocity that varies with grid size was introduced besides commonly used voidage, which means the grid size was taken into account implicitly, and so was the dynamic factor of the structure, by allowing variation of slip velocity. That may be one of the reasons why the Model M predicts an almost grid-independent solution. More details should be referred to (Wang *et al*., 2010b) to understand why it is not sufficient to take into account the meso-scale structure effects only by using a function of voidage.

To verify this domain-size dependency, the Model M was further applied in a larger periodic domain ($3 \times 12\,\mathrm{cm}^2$) for FCC particles. Figure 7 shows the comparison between the results in Figure 5b and those of larger domain ($3 \times 12\,\mathrm{cm}^2$). It is clear that larger domain leads to higher slip velocity and then lower drag coefficient, which is in agreement with our expectation and the other research results (Agrawal *et al*., 2001; Wang, 2008). Again, we can find across the whole range of grid size that the Model M predicts almost unchanged value of slip velocity,

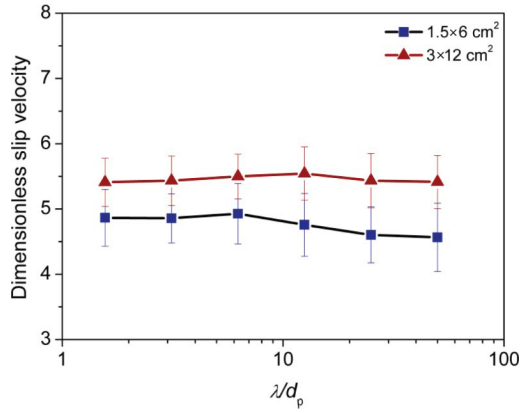

Figure 7 Effect of the periodic domain size on the time-averaged dimensionless slip velocity (u_s/u_T) with Model M. Geldart group A particles. The red triangles denote the cases with respect to the domain size of $3 \times 12\ cm^2$ and the blue squares $1.5 \times 6\ cm^2$

confirming that the Model M accurately captures the mechanism behind the structure.

It should be noted that, Model G and Model M predict quite different values of slip velocities, though their resolved structure may look similar, as shown by insets of Figure 5. Extending this seeming inconsistency to larger scales, we may expect that, simulations of real reactors with Model G and Model M may predict different solids flux even with similar impression of structures. Then, it is natural to question, which solution of these two models coincides with the reality. To answer this question, simulations of CFB risers are needed to test which will agree with experiments.

2.3.3.2 Simulations of risers and validations. Two CFB risers were selected. One is the IPE riser, with inner diameter of 90 mm and height of about 105 m and FCC particles fluidized (Li and Kwauk, 1994). The other was constructed by the group of Lothar Reh in ETH (Herbert *et al.*, 1999), with inner diameter of 411 mm and height of 8.5 m and glass beads fluidized, whose configuration has been detailed in literature (Zhang *et al.*, 2008). In simulations, the solids fluxes were not given, instead, the solids entrained out of the risers were circulated into the inlets to keep the solids inventories constant.

Figure 8 compares Model M with Model G in terms of their predictions of the axial profiles of voidage under various grid resolutions. For FCC particles, when using Model G, the solids were distributed uniformly across the riser height. It seems that the grid refining has little

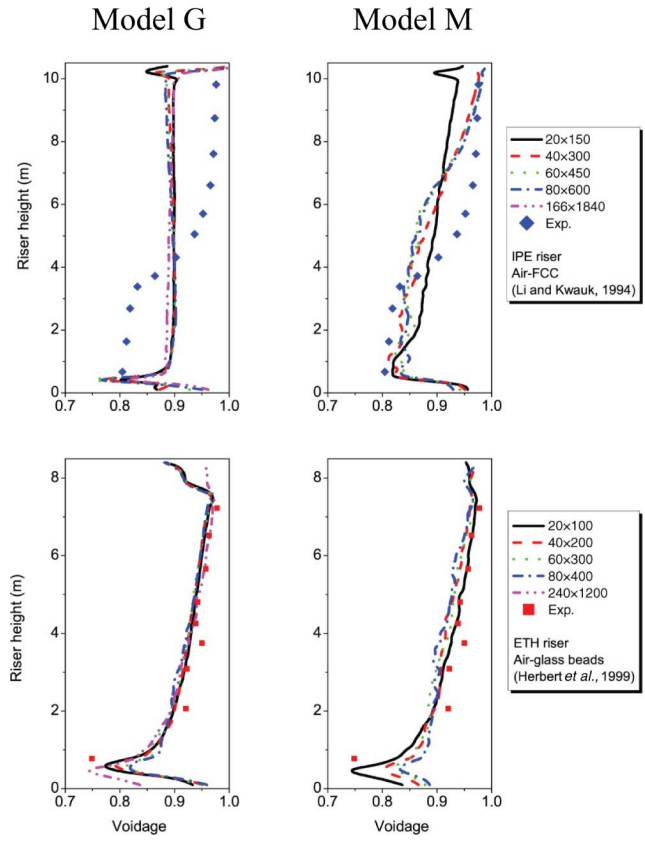

Figure 8 Axial profiles of cross-sectionally averaged voidage under different grid resolutions for IPE and ETH risers.
(Adapted from Lu **et al.**, 2009, 2011.)

effects for this case. Moreover, the predicted profiles deviate from the experimental data significantly, owing to its overpredicted drag coefficient. The prediction improves when using Model M, by which the characteristic S-shaped profile of voidage—a dilute top coexisting with a dense bottom in the axial direction—was reproduced. The solids flux was also overpredicted when using Model G, its time-averaged value was around 170 kg/(m^2 s), about 10 times the experimental data of 14.3 kg/(m^2 s). Updating to Model M improves very much, with its predicted solids flux at around 19 kg/(m^2 s) and close to reality. In addition, such improvements have been found also applicable to the other riser cases (Lu *et al.*, 2009).

For glass beads in the ETH riser, the macro-scale structures seem to be similar for different approaches, as the predicted voidage profiles

using both drag models agree well with the experimental data. However, their predicted solids fluxes still differ much from each other—the Model G predicts values near 400 kg/(m^2 s), which is about three times higher than the measured data (151 kg/(m^2 s)); while the Model M predicts values around 147 kg/(m^2 s), which are in good agreement with the data. The other comparisons in terms of radial profiles of solids distribution were also found in favor of the Model M. So, it seems that the evaluation based on the time-averaged axial profiles of solids distribution is insufficient; the circulating solids flux, which represents the dynamic characterization of the structures at the macro-scale, should be additionally examined, to judge whether an approach correctly captures the two-phase flow behavior. From the above analysis we can see that, at least for the current cases, the conventional TFM seems inadequate to describe gas–solids riser flows featuring multi-scale heterogeneity while EMMS-based multi-scale CFD improves its accuracy greatly.

2.3.3.3 Scope of applications. In literature, there are some other reports concerning the scope of applying various types of multi-scale CFD. For example, Benyahia (2010) found that the subgrid drag coefficients obtained from filtered drag model (Igci *et al*., 2008) and EMMS model (Yang *et al*., 2004) are both needed and useful in large-scale simulations. The solids used in his riser are also FCC particles, but heavier (1712 kg/m^3). The riser was operated under higher gas velocity (5.2 m/s) and higher solids flux (489 kg/(m^2 s)). Wang *et al*. (2009) addressed the applicability of TFM for bubbling fluidized bed by comparing it with discrete particle model (DPM) results. They reported that TFM can predict the correct bed expansion even without drag modifications, provided that a sufficiently fine-grid size and small time step is used. Based on scale separation analysis, Wang and Li (2007) have ever addressed that for dense gas–solids flow or bubbling fluidized beds, the subgrid structure modeling may be not needed (or not that important), but for comparatively dilute CFB, it is necessary. By and large, we may say that there are different application scopes for the correlative and the variational types of multi-scale CFD. In appearance, these differences are related with the operating conditions and physical properties of the investigated systems. As to the underlying mechanism, more efforts are still needed, and a tentative explanation may start from the scale separation analysis, as follows.

For the gas–solids two-phase flow in a CFB riser, there is no clear separation between the micro-scale (fine-grid scale of TFM continua) and the meso-scale (cluster scale), as discussed in Goldhirsch (2003) and Wang and Li (2007). Thus, the meso-scale structure does not vanish

with grid refining of TFM. That is to say, there are certain subgrid terms that cannot be solved under the conventional framework of TFM. That is probably the reason why the fine-grid simulations of risers in Figure 8 fail to predict the circulating solids flux. If the EMMS-based Model M was used instead, there will be intrinsic structure terms in the conservation equations, in the sense that the conservation applies to both the dense phase and the dilute phase, respectively. That allows capturing the intrinsic structures. For bubbling fluidized beds or some other dense flow cases, the micro-scale and the meso-scale may be separated clearly as analyzed in Wang and Li (2007). That is to say, the meso-scale structure is larger than the grid size with its characteristic relaxation time longer than computational time step. In that case, fine-grid TFM may be sufficiently precise to capture all the meso-scale structure and then no modification to the conventional drag coefficient is needed.

In summary, we may expect that the correlative type of multi-scale CFD can be used for the problems with clear scale separations between the micro-scale and the meso-scale, while the variational type, provided with appropriate stability condition, seems free of such limitation. In what follows we will detail some examples of the variational approach by introducing its basis of the EMMS model.

3. MESO-SCALE MODELING—THE KEY TO MULTI-SCALE APPROACHES

3.1 Energy-minimization multi-scale (EMMS) model—a meso-scale model

The EMMS model was first proposed for the hydrodynamics of concurrent-up particle–fluid two-phase flow. Though it is based on a rather simplified physical picture of the complex system (Li, 1987; Li and Kwauk, 1994), it harnesses the most intrinsic complexity in the system, the meso-scale heterogeneity, and this is why it allows better predictions to the critical phenomena in the system which is obscured in other seemingly more comprehensive models.

In this model, instead of the uniform and interpenetrating continuous phases of the gas and the solids, a distinct heterogeneous structure is assumed. The elemental volume in the flow field, which has displayed observable heterogeneity, is partitioned into fractions occupied by the gas-rich, dilute phase (denoted by subscript ''f'') and the particle-rich, dense phase (denoted by subscript ''c''), respectively. Within each ''phase,'' uniformity is assumed, and the dense ''phase'' is assumed to occur as spherical clusters. That is, the dense phase is discrete, surrounded by the continuous dilute phase. In this way, eight variables

is needed to define its steady state, namely, the superficial particle and fluid velocities of the dense and dilute phases (U_{pc}, U_{pf} and U_{gc}, U_{gf}), the voidages in each phase (ε_c and ε_f), the volume fraction of the dense phase (f), and the cluster diameter of the dense phase (d_c).

To facilitate the discussion in the rest part of this article, we revisit the formulation of the EMMS model, while interested readers are referred to Li and Kwauk (1994) and Li *et al*. (2005) for more details.

1. Dilute-phase momentum balance: all effective particle weight in unit dilute-phase volume is balanced by the fluid drag:

$$\frac{3}{4}C_{Df}\frac{1-\varepsilon_f}{d_p}\rho_g U_{sf}^2-(1-\varepsilon_f)(\rho_p-\rho_g)g=0, \tag{1}$$

where $U_{sf}=U_{gf}-U_{pf}f/(1-f)$ is defined as the dilute-phase superficial slip velocity.

2. Dense-phase momentum balance: effective particle weight in unit dense-phase volume is partially supported by the dense-phase fluid flow, and the rest is supported by the bypassing dilute phase fluid flow,

$$\frac{3}{4}C_{Dc}\frac{1-\varepsilon_c}{d_p}\rho_g U_{sc}^2 f+\frac{3}{4}C_{Di}\frac{f}{d_c}\rho_g U_{si}^2-f(1-\varepsilon_c)(\rho_p-\rho_g)g=0. \tag{2}$$

3. Pressure balance between dense and dilute phases: the dense phase pressure drop is balanced by that of the dilute phase plus the ''interphase,''

$$C_{Df}\frac{1-\varepsilon_f}{d_p}\rho_g U_{sf}^2+\frac{f}{1-f}C_{Di}\frac{1}{d_c}\rho U_{si}^2-C_{Dc}\frac{1-\varepsilon_c}{d_p}\rho_g U_{sc}^2=0. \tag{3}$$

4. Continuity of the fluid phase:

$$U_g=fU_{gc}+(1-f)U_{gf}. \tag{4}$$

5. Continuity of the solids:

$$U_p=fU_{pc}+(1-f)U_{pf}. \tag{5}$$

6. Cluster diameter:

$$\frac{d_c}{d_p}=\frac{((\rho_p-\rho_g)gU_p)/\rho_p(1-\varepsilon_{max})-N_{st,mf}}{N_{st}-N_{st,mf}}, \tag{6}$$

where ε_{max} denotes the maximum voidage existent for heterogeneous particle–fluid flow (Matsen, 1982) and the subscript ''mf'' denotes the state of minimum fluidization. N_{st} is the energy consumption for suspending and transporting the solids with respect to unit mass, which can be calculated from

$$N_{st} = \frac{W_{st}}{(1-\varepsilon_g)\rho_p} = \frac{\rho_p - \rho_g}{\rho_p}\left[U_g - \frac{\varepsilon_f - \varepsilon_g}{1-\varepsilon_g} f(1-f)U_{gf}\right]g, \qquad (7)$$

where

$$N_{st,mf} = \frac{\rho_p - \rho_g}{\rho_p}\left(U_{mf} + \frac{U_p \varepsilon_{mf}}{1-\varepsilon_{mf}}\right)g. \qquad (8)$$

These six equations are insufficient to give a closure of the EMMS model that involves eight variables. The closure is provided by the most unique part of the EMMS model, that is, the introduction of stability condition to constraint dynamics equations. It is expressed mathematically as $N_{st} = \min$, which expresses the compromise between the tendency of the fluid to choose an upward path through the particle suspension with least resistance, characterized by $W_{st} = \min$, and the tendency of the particle to maintain least gravitational potential, characterized by $\varepsilon_g = \min$ (Li and Kwauk, 1994).

A direct application of the model and demonstration of its predictability is the prediction of choking point in fast-fluidization. The abrupt change in particle concentration in the risers of circulating fluidization beds with the continuous variation of gas or solids flux has long been a controversial issue. With the EMMS model, it is now apparent that regime transition is related to this phenomena where the dominant mechanism in the system shifts from particle–fluid compromising to fluid dominating (Li and Kwauk, 1994), and mathematically, it is a jump between two branches of the stable solution (Ge and Li, 2002), as shown in Figure 9. This ability of the EMMS model has shown its practical significance in the designing and scaling-up of industrial fluidization systems as will be discussed in more detail later.

3.2 Coupling of EMMS and CFD

The EMMS model was proposed for the time-mean behavior of fluidized beds on the reactor scale. A more extensive application of the EMMS model to gas–solid flow is through its coupling with the two-fluid CFD approaches, which brings about an EMMS-based multi-scale CFD framework for gas–solid flow. For this purpose, Yang *et al*. (2003) introduced an acceleration, a, into the EMMS model to account for the

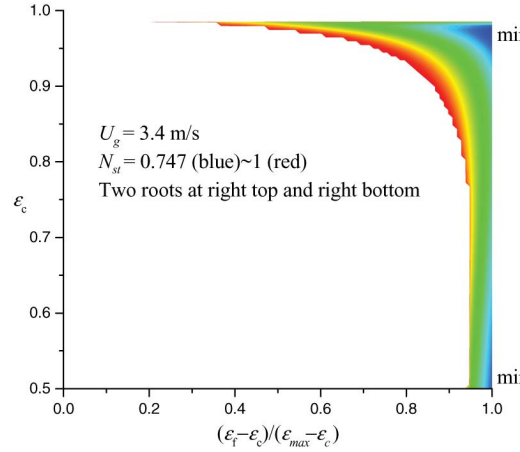

Figure 9 Variation of N_{st} with ε_c and ε_f for the FCC–air system (G_s = 50 kg/(m^2 s)). Two minimum points in blue correspond to the dilute and the dense flow, respectively, and their coexistence corresponds to the choking state of fluidization (Ge and Li, 2002).

force imbalance between the effective gravity of particles and the drag force, and the local voidage was also introduced as a new known quantity. In this way, a simplified structure-dependent drag coefficient was proposed, and it was found being able to greatly improve the TFM prediction in terms of the axial profiles of voidage as well as the circulating solids flux. Without EMMS correction, the conventional TFM simulation was found to overpredict the solids flux by almost 10 times, while the EMMS-based approach correctly predicts the solids flux and the axially S-shaped profiles of voidage (Yang *et al*., 2004).

Later on, based on the in-depth understanding of the applicability of the stability condition (Li *et al*., 2004; Zhang *et al*., 2005), the EMMS model was extended, to describe the meso-scale structures at the sub-grid level (Wang and Li, 2007). In more detail, first, as mentioned above for the challenges to the variational type of multi-scale CFD, though the hydrodynamic conservation equations were established on the micro-scale of continuum, the stability condition of the EMMS model was found applicable only to the higher meso-scales (Li *et al*., 2004). Such a mismatch of scales is the main problem encountered in coupling EMMS and TFM. To coordinate the hydrodynamics and the stability condition at different scales, the extended EMMS model (named after EMMS/matrix) adopts a two-step scheme, as follows:

Step 1:

The first step is to determine the meso-scale parameters in terms of the diameter and voidage of clusters (d_c and ε_c) with the constraint of the

global stability condition $N_{st} \rightarrow \min$. These two parameters are the time-mean characterization of the clusters, leaving the fluctuating information to the second step in terms of velocities and accelerations. The relevant momentum conservation equations in the first step are as follows (strictly speaking, the parameters in Step 1 are cross-sectionally averaged variables, and should be bracketed with $< >$. For simplicity, we neglect these angle brackets):

$$\Phi_1(X) = \frac{3}{4}\frac{1-\varepsilon_c}{d_p} C_{\mathrm{Dc}} \rho_g |U_{\mathrm{sc}}| U_{\mathrm{sc}} - (1-\varepsilon_g)(\rho_p - \rho_g)(a_c + g) = 0, \quad (9)$$

$$\Phi_2(X) = \frac{3}{4}\frac{1-\varepsilon_f}{d_p} C_{\mathrm{Df}} \rho_g |U_{\mathrm{sf}}| U_{\mathrm{sf}} - (1-\varepsilon_f)(\rho_p - \rho_g)(a_f + g) = 0, \quad (10)$$

$$\Phi_3(X) = \frac{3}{4}\frac{f}{d_c} C_{\mathrm{Di}} \rho_g |U_{\mathrm{si}}| U_{\mathrm{si}} - f(\rho_p - \rho_g)(\varepsilon_g - \varepsilon_c)(a_i + g) = 0, \quad (11)$$

where the pressure drop balance assumption relates a_{i} with the other two inertial terms by

$$a_i = \frac{(1-f)[(1-\varepsilon_g)(a_c+g) - (1-\varepsilon_f)(a_f+g)]}{f(\varepsilon_g - \varepsilon_c)} - g. \quad (12)$$

The mass conservation equations of the gas and particles are the same with the original, as follows:

$$\Phi_4(X) = U_p - U_{\mathrm{pf}}(1-f) - U_{\mathrm{pc}} f = 0, \quad (13)$$

$$\Phi_5(X) = U_g - U_{\mathrm{gf}}(1-f) - U_{\mathrm{gc}} f = 0. \quad (14)$$

The average voidage ε_{g} relates ε_{f} and ε_{c} by

$$\Phi_6(X) = \varepsilon_g - f\varepsilon_c - (1-f)\varepsilon_f = 0. \quad (15)$$

The definition of cluster diameter d_{c} remains the same with the original (Equation (6)), which read

$$\Phi_7(X) = \frac{d_c}{d_p} - \frac{((\rho_p - \rho_g) g U_p)/(\rho_p(1-\varepsilon_{\max})) - N_{\mathrm{st,mf}}}{N_{\mathrm{st}} - N_{\mathrm{st,mf}}} = 0, \quad (16)$$

where the energy consumption for suspending and transporting particles, $N_{\mathrm{st}} = \min$, as is in the original form.

It should be noted that if the inertial terms are omitted, the above relations will return to the original form of the EMMS model (Li and Kwauk, 1994). For specified conditions U_{g}, G_{s}, and ε_{g}, this set of 10

variables $\mathbf{X} = (U_{gc}, U_{pc}, U_{gf}, U_{pf}, \varepsilon_f, \varepsilon_c, f, d_c, a_c, a_f)$ in the model can be determined by satisfying seven equations, $\boldsymbol{\Phi}(\mathbf{X})$, under constraint of the minimization of N_{st}. These seven equations are nonlinear; their solution follows a scheme that is similar to that used for the original EMMS model, whose detail is referred to Wang and Li (2007). With the above scheme, the variation of d_c and ε_c can be determined as functions of cross-sectionally averaged voidage $<\varepsilon_g>$. In practice, at least for Geldart A particles, $N_{st} \to \min$ requires the maximization of ε_f and minimization of a_f, that is, $\varepsilon_f \to \varepsilon_{max}$ and $a_f \to -g$. Such two relations can be used to reduce the computation. Alternative models for d_c and ε_c may be expected to improve the EMMS-based models; one of such efforts can be referred to the work of Wang *et al*. (2008a).

Step 2:

In the second step, d_c and ε_c are known parameters ready for using. The EMMS model is coupled with TFM in this step—with input from CFD results, that is, the gas and solids velocities ($\boldsymbol{u}_g$ and $\boldsymbol{u}_p$) and voidage ε_g in each grid, the remaining variables of EMMS, that is ($\boldsymbol{U}_{gc}, \boldsymbol{U}_{pc}, f$) for the dense phase and ($\boldsymbol{U}_{gf}, \boldsymbol{U}_{pf}$) for the dilute phase as well as the inertial terms associated to each phase, can be determined to supply the subgrid structure parameters for calculating the drag coefficient. The algorithm is similar to the step 1, but can be simplified according to the relative invariance, by reorganizing the conservation equations as functions of slip velocities (Lu *et al*., 2009). After simplification, only three unknown variables ($\boldsymbol{U}_{sc}, \boldsymbol{U}_{si}, a_c$) are needed to solve and the relevant equations are as follows:

$$\frac{3(1-\varepsilon_c)}{4d_p} C_{Dc} \rho_g |\boldsymbol{U}_{sc}| \boldsymbol{U}_{sc} = (\rho_p - \rho_g)(1-\varepsilon_g)(\boldsymbol{a}_c - \boldsymbol{g}), \tag{17}$$

$$\frac{3}{4d_c} C_{Di} \rho_g |\boldsymbol{U}_{si}| U_{si} = (\rho_p - \rho_g)(\varepsilon_g - \varepsilon_c)(\boldsymbol{a}_i - \boldsymbol{g}), \tag{18}$$

$$\boldsymbol{U}_{si} = (\boldsymbol{U}_s - f\boldsymbol{U}_{sc}) \frac{\varepsilon_f (1-\varepsilon_g)}{\varepsilon_f - \varepsilon_g}. \tag{19}$$

The EMMS-based drag coefficient was calculated by

$$\beta = \frac{(\rho_p - \rho_g)\varepsilon_g^2}{\boldsymbol{U}_s} (1-\varepsilon_g)(\boldsymbol{a}_c - \boldsymbol{g}). \tag{20}$$

Here the vector division results in a scalar and the vectors on both numerator and denominator have the same orientation. The relevant algorithm should be referred to Lu *et al*. (2009).

Strictly speaking, the values of d_c and ε_c used in the step 2 should be calculated as functions of the cross-sectionally averaged voidage $\langle\varepsilon_g\rangle$, as the step 1 of the algorithm is performed with global operating conditions. In practice, however, correlating them with local voidage was found only have trivial effects on the final prediction. So, for simplicity, we may use local voidage in simulations (Lu *et al.*, 2009).

Following the above scheme, we can calculate a structure-dependent drag coefficient. To compare with the correlations in literature, we take the homogeneous drag coefficient β_0 from Wen and Yu (1966) as the scale and define the heterogeneity index H_D with ($H_D \equiv \beta/\beta_0$). Here β refers to all the other drag coefficients. As shown to the left of Figure 10, there are big discrepancies up to several orders of magnitude on the current correlations. By comparison, the right-hand side of Figure 10 shows a typical surface of H_D calculated with EMMS/matrix for an air–FCC system as a function of local Reynolds number Re_p and voidage. For visualization, only the vertical slip velocity is used here. It is obvious that the meso-scale modeling results in significant variation that covers the range of difference in literature, and therein the voidage appears to be the dominant factor. In most of the range of voidage, gas, and solids tend to ''compromise'' to reach each of their dominance. That is, the particles tend to aggregate for least gravity potential and the gas tend to flow around aggregates with least resistance. In this way, the gas–solids interphase momentum transfer decreases and then the effective drag coefficient is less than that for homogeneous suspensions (i.e., $H_D < 1.0$). At the two ends of voidage spectrum, H_D approaches unity corresponding to the homogeneous states of packed bed and extremely dilute flow, where two-phase ''compromise'' gives way to particle dominance and gas dominance, respectively. Higher slip velocity

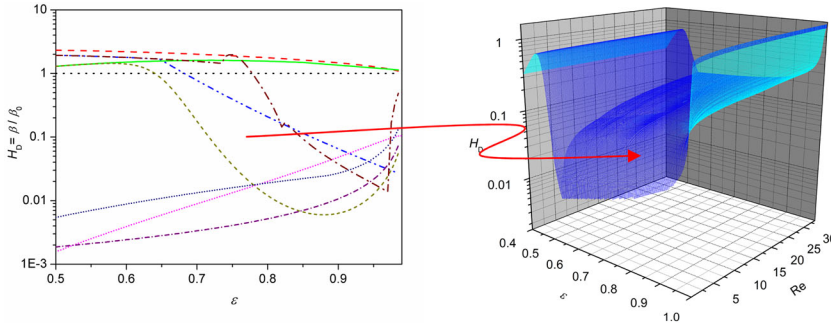

Figure 10 A tentative answer to disputes on drag coefficient with a typical surface of the heterogeneity index for a FCC–air system (ρ_p = 930 kg/m^3, d_p = 54 m, U_g = 1.52 m/s, G_s = 14.3 kg/(m^2 s), ε_{mf} = 0.4, ε_{max} = 0.9997).

means gas dominance is strengthened and then formation of aggregates is suppressed, leading to higher values of H_D. In practice, for the dilute flow in large-scale gas-fluidized beds, for example, CFB boilers, the gas turbulence may have important effect on the two-phase flow distribution, and thus, the dominant mechanisms accounting for turbulence may need to be considered (Li *et al.*, 1999). A preliminary attempt to include this effect can be referred to Lu (2009) for CFB boiler modeling.

Figure 11 shows some simulation results of the above-mentioned ETH CFB using the EMMS/matrix model (Zhang *et al.*, 2008). The simulation was performed on 3D, full-loop geometry. To the left is a snapshot of the solids distribution at the wall. Axial coexistence of a dilute top and a dense bottom can be clearly seen in the riser, with clusters falling along the riser wall as well as in the cyclone. A dense bottom was also formed in the downer side, where the higher pressure drives solids recycling through the siphon valve to the riser. The next to the snapshot shows an axial profile of the cross-sectionally averaged solids volume fraction. The right-hand side shows the radial profiles of the time-average solids volume fraction and the time-average solids velocity. In general, the simulation agrees well with the experimental

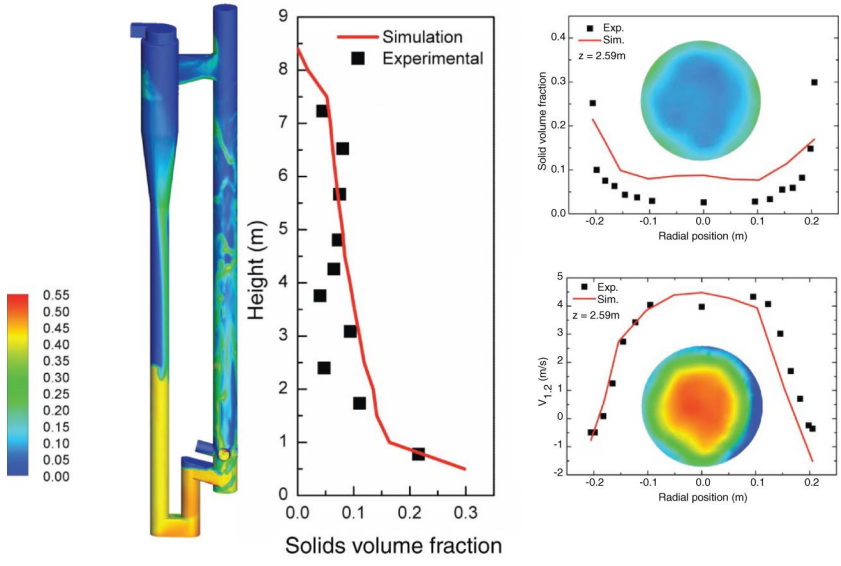

Figure 11 A typical snapshot of the simulated solids distribution at the wall of the ETH CFB, along with the axial profile of the cross-sectionally averaged solids volume fraction and the radial profiles of time-average solids volume fraction and solids velocity ($\rho_p = 1400$ kg/m^3, $d_p = 60$ m, $U_g = 3.5$ m/s, $H_0 = 1.7$ m).
(Adapted from Zhang **et al.**, 2008.)

data. The characteristic core-annulus structure in radial direction is also captured. It should be noted that, for this case, the grid size is around 9 mm in radial direction, which is about 150 times the particle diameter. That meshing is rather coarse for the conventional TFM simulation according to what has been obtained in periodic-domain simulations, as shown in Figure 5. For EMMS-based multi-scale CFD, however, the grid size is still within the acceptable range. So, we can say that the EMMS-based multi-scale CFD reduces the load of computing to a large extent.

Another merit of the EMMS-based multi-scale CFD can be represented by its ability to predict flow regime diagrams of CFB. In practice, how to situate a reactor to an appropriate regime remains a critical issue for both design and operating. Running in an inappropriate flow regime may cause severe instability. Figure 12 shows calculated flow regime diagrams in forms of a series of iso-ug, which relates the solid flux G_s with the total pressure drop of riser at specified superficial gas flow rate U_g. Some characteristic snapshots of solids distribution are also drawn as insets. To the left is the diagram for an air–FCC system that is calculated with the simplified EMMS drag model (Yang *et al.*, 2003), while to the right is that for an air–HGB (hollow glass beads) system that is calculated with EMMS/matrix model. At least three regimes can be distinguished in these two diagrams, that is, the dilute transport, the dense upflow and in between the ''choking'' or the ''continuous'' transitions. The coexistence of the dense upflow with the dilute transport marks the choking, which occupies the bell-shaped areas where the iso-ug levels off with G_s equal to the saturation carrying capacity. The summit of the bell-shaped area can be named after the ''critical point,'' above which the continuous nonchoking transitions bridges between

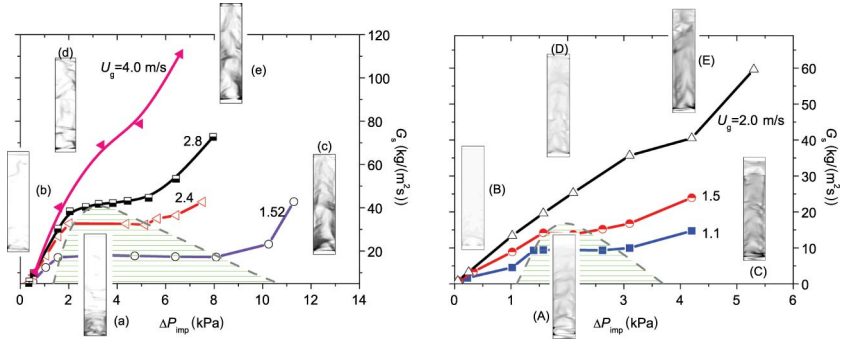

Figure 12 Calculated flow regime diagrams for an air–FCC (d_p = 54 m, ρ_p = 930 kg/m^3) system and an air–HGB (hollow glass beads, d_p = 75 m, ρ_p = 609 kg/m^3) system (Wang *et al.*, 2008).

the dilute transport and the dense upflow. Quantitative comparison also manifests good agreement between this simulated regime diagram and the experimental (Li *et al*., 2007; Wang *et al*., 2007).

The flow regime in Figure 12 is an ''apparent flow regime'' (Wang *et al*., 2008) in that it is associated with not only hydrodynamics but also geometric factors. It was found that this apparent flow regime changes gradually with the riser height (Li and Kwauk, 1994; Wang *et al*., 2008), as shown in Figure 13a. Higher riser reduces the inlet/outlet effects and has a higher ratio of riser height for a flow state to be fully developed, thus leading to wider area for the choking transition. A short riser whose whole length is affected by the inlet/outlet effect may be hard to discern the choking transition. Recent experiments on a cold model of CFB boiler validate this tendency (Hu *et al*., 2009).

The flow regime that is purely defined by hydrodynamics was named after the ''intrinsic flow regime'' (Wang *et al*., 2008). Figure 13b gives the intrinsic flow regime diagram calculated with the original EMMS model for the air–FCC system. Similar partitions of the flow regimes can be distinguished over the investigated range of G_s and the averaged solids volume fraction ε_{s0} ($\varepsilon_{s0} = \Delta P_{imp}/(\rho_p g H)$). Clearly, the intrinsic choking transition area is sloping and larger than that of the apparent one.

Comparing the apparent and the intrinsic diagrams in Figure 13, we may conclude that, the apparent flow regime and the choking transition area change with the riser height. Accordingly, the critical point will rise to a higher position with increase of riser height. The upper limit of this expansion is the intrinsic flow regime that is purely defined by

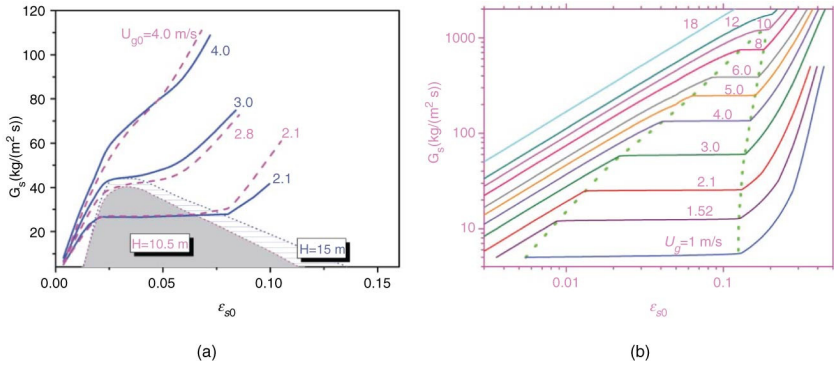

Figure 13 The apparent flow regime diagram calculated with EMMS-based multiscale CFD and the intrinsic flow regime diagram for the air–FCC system (fluid catalytic cracking particle, $d_p = 54$ m, $\rho_p = 930$ kg/m^3) calculated by using the EMMS model without CFD. The intrinsic flow regime diagram is independent of the riser height (Wang *et al*., 2008).

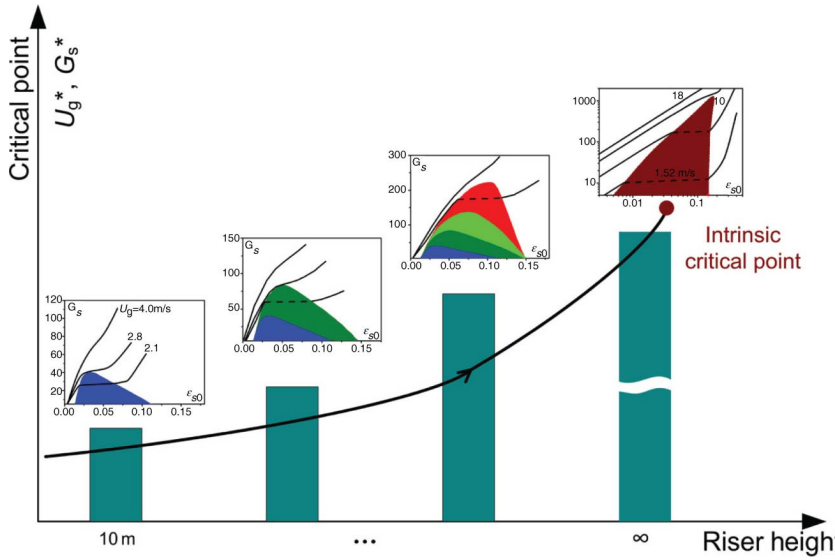

Figure 14 Riser height decides the variation from apparent to intrinsic flow regime diagrams. Dark cyan columns represent different riser heights with relevant flow regime diagram sketched above, and the curve denotes the variation of the critical point with the final end of intrinsic critical point (Wang *et al*., 2010b).

hydrodynamics, as depicted in Figure 14. In our opinion, this dependency of the flow regime on the riser height is at least one of the major reasons that cause disputes in literature (say, e.g., the review articles of Bi *et al*., 1993 and Yang, 2004) about understanding the choking phenomena. In practice, different research groups perform choking studies with different designs of CFB in terms of riser height and the other geometric factors. As a result, different understanding of the choking occurs with different quantifications of their apparent flow regime transitions. It is very hard, if not impossible, to unify all the experimental findings from different research groups, or to perform experiments getting rid of all the geometric factors. The solution to this puzzle may be twofold: one is to add an axis of the riser height (some other geometric factors may also affect) to the flow regime diagram, to allow understanding the complex interrelations between hydrodynamics and geometric limitations. We called this diagram the ''operating diagram'' (Wang *et al*., 2008). The other is to study these phenomena through virtual experiments of a series of 3D, full-geometry simulations of CFB, as the virtual experiments are much easier to control the manifold factors and also getting more reliable and cheaper with rapid development of computing technologies. Our recent attempt has unfolded the

latter approach with fresh insight (Zhang *et al*., 2008). More efforts are expected to finally reach the common knowledge of the flow regime transitions of CFB.

3.3 Application of EMMS to mass/heat transfer and reactions

Meso-scale structure significantly affects the mass transfer but receives less research attention. The first reason for this ignorance lies in that the mass transfer is coupled with the momentum transfer, making its dependency on the structure more complicate. Available few efforts show that the determination of the mass transfer rate, either experimental or theoretical, is difficult, especially with variation of dynamic structure (Wang, 2002; Wang *et al*., 2005; Yu and Jin, 1994). The second reason may relate with the underestimation of the relative role of the mass transfer on the overall reaction rate. For a CFB reactor, fine particles with large specific area react to the surrounding gas under high slip velocity. It is normally expected in such a case, the fluid–particle mass transfer rate is very high and therefore the overall reaction rate is controlled by the other lower rate steps such as the intrinsic reaction rate. For example, if the ozone decomposition on a FCC particle was modeled, its reaction coefficient k_r was reported of the order of magnitude of $10\ s^{-1}$, while the overall mass transfer coefficient $k_p\alpha_p$ was of the order of $10^5\ s^{-1}$ (Dong *et al*., 2008a; Ouyang *et al*., 1995), then the difference of four orders of magnitude can be expected using such micro-scale analysis and that ($Da = k_r/k_p\alpha_p \ll 1$) means the mass transfer modeling is negligible. However, the meso-scale structure may reduce the overall mass transfer rate, in the same way as it affects the drag coefficient, making $Da \sim 1$. The last but not the least reason lies in that the intrinsic reaction rate for the most of heterogeneous systems is hard to measure. For example, the combustion of a char particle may relate with manifold factors such as devolatilization, attrition and inner diffusion inside the ash layers, and so on, while each of these processes is very hard to present a generalized model. For petroleum refinery processes as another example, the complex network may involve hundreds or even thousands of elementary reactions that are very hard to determine. As a result, we are short of the intrinsic reaction rate data, and this situation directly hinders the application of mass transfer modeling.

The meso-scale structure promotes gas bypassing clusters, and thus, decreases the effective interphase mass/heat transfer rate. Following the EMMS model for resolving the structure, a multi-scale mass transfer model, EMMS/mass (Dong *et al*., 2008a, 2008b), was proposed. With the two-phase structures calculated from the EMMS/matrix model, the gas concentration in the dense phase and in the dilute phase were distinguished at the subgrid level. The mass conservation equations for these

two subgrid continua were then derived in a way similar to the conventional equations for mixture concentrations, as follows:

Mass conservation for the gas mixture:

$$\frac{\partial}{\partial t}(\phi_k \varepsilon_k \rho_g) + \nabla \cdot (\phi_k \varepsilon_k \rho_g \boldsymbol{u}_{\mathrm{gk}}) - S_k - \Gamma_k = 0. \tag{21}$$

Mass conservation of component A in the gas mixture:

$$\frac{\partial}{\partial t}(\phi_k \varepsilon_k \rho_g Y_{\mathrm{Ak}}) + \nabla \cdot (\phi_k \varepsilon_k \rho_g Y_{\mathrm{Ak}} \boldsymbol{u}_{\mathrm{gk}} - \phi_k \varepsilon_k \rho_g D_m \nabla Y_{\mathrm{Ak}}) - S_k - \Gamma_{\mathrm{Ak}} = 0, \tag{22}$$

where subscript k denotes the phase k (k = c, dense phase; k = f, dilute phase); the volume fraction ϕ_{k} is f or $(1 - \mathrm{f})$ for the dense phase or dilute phase; Y_{Ak} denotes the mass fraction of A in the phase k, and it relates with the averaged concentration by

$$\varepsilon_g \rho_g Y_A = \sum_{k=c,f} (\phi_k \varepsilon_k \rho_g Y_{\mathrm{Ak}}). \tag{23}$$

D_{m} denotes the molecular diffusion coefficient; Γ_{k} denotes the interphase mass exchange rate between the dense and the dilute phases and $\Gamma_{\mathrm{c}} = -\Gamma_{\mathrm{f}}$, which can be directly calculated with EMMS/matrix model parameters if the reaction source term, S_{k}, is negligible compared to the bulk gas conservation. For vaporization of A, the source term reads

$$S_k = \phi_k k_k (1 - \varepsilon_k) \alpha_p \rho_g (Y_{\mathrm{A,sat}} - Y_{\mathrm{Ak}}), \tag{24}$$

where k_{k} denotes the mass transfer coefficient between gas and particles in homogeneous suspension of phase k, and various empirical relations can be used in this regard, in which most of them take the form of Ranz relation (Ranz, 1952). The meso-scale mass exchange rate of A, Γ_{Ak}, can be approximated by two parts of contributions: one is from a stable part, just like a virtual ''big particle''; the other is from a dynamic part via cluster-interface renewal or transformation. The stable part can be calculated with the classic surface renewal theory (Bird *et al*., 1960) or the above mentioned Ranz empirical relations; the dynamic part can be approximated by $\Gamma_{\mathrm{k}} \cdot Y_{\mathrm{Ay}}$ if the interphase exchange is dominated by convection, where the subscript y denotes the phase of carrier gas. More details about the model closures are referred to Dong *et al*. (2008a).

If the reaction has little effects on the flow and the convection dominates the mass transfer, then Equations (21)–(24) can be reduced into algebraic expression of subgrid concentration of transferred component, as follows:

$$Y_{\mathrm{Ac}} = \frac{\varepsilon_g}{f \varepsilon_c} \frac{(\boldsymbol{u}_{\mathrm{gf}} - \boldsymbol{u}_g)}{(\boldsymbol{u}_{\mathrm{gf}} - \boldsymbol{u}_{\mathrm{gc}})} \cdot Y_A \tag{25}$$

$$Y_{\mathrm{Af}} = \frac{\varepsilon_g}{(1-f)\varepsilon_f} \frac{(\boldsymbol{u}_g - \boldsymbol{u}_{\mathrm{gc}})}{(\boldsymbol{u}_{\mathrm{gf}} - \boldsymbol{u}_{\mathrm{gc}})} \cdot Y_A \tag{26}$$

Such a simplified form is easier than the partial differential equations to analyze the effect of structures on the mass transfer. More details about its analysis are referred to Zhang (2010). The EMMS/mass model has been used to evaluate the overall mass transfer coefficient in a CFB riser (Dong *et al.*, 2008a). For a one-dimensional, steady state and fully developed riser, the above equations can be simplified by ignoring all the terms related with $\partial/\partial t$, $\partial/\partial r$. If the cluster variation along the riser height is further ignored, then the two-phase structure parameters (ϕ_k, ε_k, u_{gk}) can be calculated from the original EMMS model instead of the EMMS/matrix model. The final solution of the steady-state version of EMMS/mass model was plotted in Figure 15b with magenta circles for a system with naphthalene and air, having Schmidt number, Sc, at around 2.5. For comparison, Figure 15a is the experimental data in the literature drawn in conventional way, where the overall Sherwood number $\mathrm{Sh}_{\mathrm{ovr}}$ relates with the superficial Reynolds number $\mathrm{Re}_0(=U_g d_p \rho_g / \mu_g)$. Owing to the lack of description of structure (it should be noted that, sometimes, wrong interpretation models for processing the experimental data are also the causes, as discussed in Kunii and

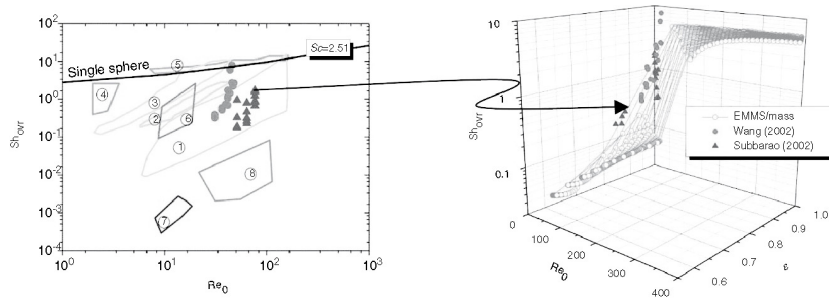

(a) Conventional correlation by Sh versus Re shows that data scatters and poorly depends on Re_0 even within one source.

(b) EMMS description of Sh unifies different sources of data and shows good agreement between model predictions and data.

Figure 15 A tentative answer to the disputes on mass transfer (adapted from Dong et al., 2008a): comparison of overall Sherwood number between this work and the literature data. (a) Conventional Sh–Re curve of (1) Subbarao and Gambhir (2002); (2) Kettenring and Manderfield (1950); (3) Resnick and White (1949); (4) Venderbosch *et al.* (1999); (5) Gunn (1978); (6) Van der Ham *et al.* (1991); (7) Dry *et al.* (1987); (8) Dry and White (1992). (b) EMMS/mass predictions of $\mathrm{Sh}_{\mathrm{ovr}}$ as a function of Re_0 and ε and its comparison with experimental data.

Levenspiel, 1991), for one specific Re_0, the data are diffused over a wide range of Sh_{ovr}. If the data are redrawn with consideration of structure, as shown in Figure 15b, we can see that the diffuse of data are due to different voidage, and the EMMS/mass model predictions agree well with these two sets of data. That can be viewed as our tentative answer or solution to the disputes over mass transfer drawn in Figure 3.

In all, Reynolds number is insufficient to correlate the overall Sherwood number in a CFB. This is the reason why the conventional correlations of mass transfer coefficient diffuse over several orders of magnitudes (Breault, 2006). Introducing structures, in terms of voidage for this case, improves very much the prediction. The abrupt change of Sherwood number at Reynolds number around 50–100 and voidage around 0.85–1.0 corresponds to the jump change of choking. It is interesting to note that the Sherwood number for classical fluidized beds and fixed beds also displays abrupt change around this range of Re_0 (Kunii and Levenspiel, 1991). Thus, one may expect that certain common mechanisms are underlying these phenomena. More efforts are needed to unify the mass transfer theory with progress in meso-scale modeling.

The full version of the EMMS/mass mass transfer model has also been coupled with CFD to show its improvement over conventional approaches for reactive multiphase flow simulations (Dong *et al.*, 2008b). Figure 16 shows the necessity of this meso-scale modeling through partial and full replacement of the conventional CFD approaches when simulating an ozone decomposition experiment (Ouyang *et al.*, 1995). The conventional CFD without any meso-scale modeling gives rather poor results in that both the interphase momentum transfer and the mass transfer rate were overpredicted and then ozone were decomposed too fast (Figure 16c). When the drag coefficient was corrected with a meso-scale model (here, EMMS/matrix) but the mass transfer model remains unchanged, the prediction was improved, more ozone being released from the top outlet instead of being totally consumed in the riser (Figure 16b). If the meso-scale modeling for mass transfer was also introduced, the prediction improved further, showing the best agreement with experimental data in terms of ozone concentration along the radial direction at two elevations (Figure 16a). In all, accurate prediction of reaction behavior greatly depends on the meso-scale structure modeling, both on mass transfer and momentum transfer. Accurate prediction can be viewed as our tentative answer to the question of reactive modeling issued in Figure 3.

With additional assumption of analogy between mass and heat transfer, which is valid for low mass transfer rate processes, similar approach has ever been proposed to model the particle–fluid heat transfer (Hou and Li, 2010). The overall heat transfer, however, may

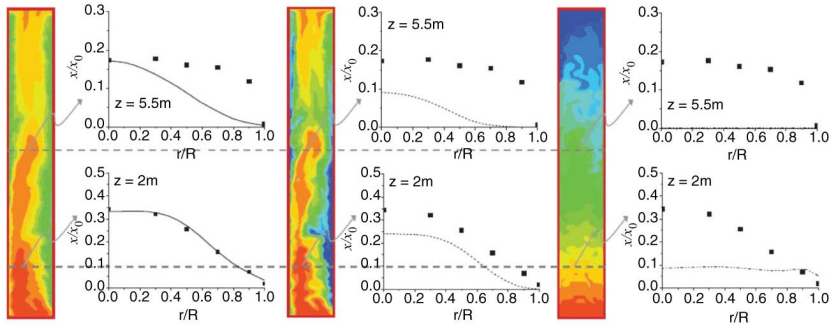

Figure 16 A tentative answer to the question on reactive modeling: snapshots of dimensionless ozone concentration at time of No. 30 s and related time-averaged radial profiles at different heights (experiment: Ouyang *et al*., 1995; $U_g = 3.8$ m/s, $G_s = 106$ kg/m^2 s, $k_r = 57.21$ m^3(O$_3$)/m^3 (catalyst)s). (a) EMMS/matrix for flow and EMMS/mass for mass transfer; (b) only flow structure is considered through a EMMS/matrix drag coefficient, mass transfer model is the conventional; (c) conventional CFD model for both flow and mass transfer without structural consideration (color spectrum is in log scale) (Dong *et al*., 2008b).

be mixed with particle–particle heat conduction in dense fluidized beds and tends to be very rapid. In contrast, the effects of meso-scale structure on the bed-to-wall heat transfer are often of engineering interest and have been investigated extensively. In a CFB combustor, the intense convection and renewal of particles in the vicinity of the wall as well as the particle–wall collisions represents the main contribution to the total bed-to-wall heat transfer. To account for this meso-scale effect, the cluster renewal model was proposed by Basu and Fraser (1991). It was assumed that any parts of the wall are in alternate contact with the cluster and dispersed particles. Assume δ is the fraction of the wall contacted with clusters, then, the overall heat transfer coefficient h can be written as

$$h = h_{\text{con}} + h_{\text{rad}} = \delta(h_{\text{c,con}} + h_{\text{c,rad}}) + (1 - \delta)(h_{\text{f,con}} + h_{\text{f,rad}}), \qquad (27)$$

where subscripts ''con'' and ''rad'' denote convection and radiation contributions, respectively. The critical parameter therein, that is, the cluster fraction δ at the wall, can be calculated with EMMS/matrix subgrid model. This is what we have adopted in simulating an industrial CFB boiler (Wang and Li, 2010; Zhang, 2010), as will be detailed in industrial applications in Section 4.

3.4 Extension of EMMS modeling to gas–liquid flow

Albeit originally proposed for gas–solid fluidization, the concepts of structure resolution and compromise between dominant mechanisms embodied in the EMMS model can be generalized into the so-called variational multi-scale methodology (Li and Kwauk, 2003) and extended to other complex systems (Ge *et al.*, 2007). One typical example out of these extensions is the Dual-Bubble-Size (DBS) model for gas–liquid two-phase flow in bubble columns (Yang *et al.*, 2007, 2010).

Analogous to the EMMS model, the gas–liquid systems in bubble columns can be resolved physically into small bubbles, large bubbles, and liquid phase. Note that the significance of this ''structure'' resolution lies not only in the classification of different phase structure but in the differentiation of different dominant mechanisms that can be mathematically expressed as various extremum tendencies. When larger bubbles break into smaller daughter bubbles, the energy dissipated for bubble surface oscillation and deformation (N_{surf}) decreases. This process is governed by $N_{\mathrm{surf}} \rightarrow \min$, and hence the global two-phase flow field in this case is taken over by the liquid phase. On the other hand, when smaller bubbles coalesce into larger bubbles, the energy dissipation through liquid turbulence (N_{turb}) decreases. The process is dominated by $N_{\mathrm{turb}} \rightarrow \min$ to favor the formation of large bubbles and the global two-phase flow field in this case is therefore dominated by gas phase. However, bubbles may break up at one location and coalesce at another, and the dynamic balance between the two dominant mechanisms is usually well established in practical industrial systems, which can be expressed with a stability condition $N_{\mathrm{surf}} + N_{\mathrm{turb}} \rightarrow \min$ (Ge *et al.*, 2007; Yang *et al.*, 2010; Zhao, 2006).

From the multi-scale point of view, the total energy dissipation N_{T} can be grouped into three portions, namely, N_{surf}, N_{turb}, and N_{break}. The last portion is generated from bubble breakage and finally dissipated in the process of bubble coalescence. While N_{surf} and N_{turb} are considered to be directly dissipated on micro-scale, N_{break} is counted as a kind of meso-scale energy dissipation. Therefore, the stability condition can be either expressed with the minimization of micro-scale energy dissipation $N_{\mathrm{surf}} + N_{\mathrm{turb}} \rightarrow \min$ or conveyed as the maximization of meso-scale energy dissipation $N_{\mathrm{break}} \rightarrow \max$.

With such an understanding on system complexity in mind, the DBS model is composed of two simple force balance equations, respectively, for small or large bubble classes, and one mass conservation equation as well as the stability condition serving as a variational criterion and a closure for conservative equations. For a given operating condition of the global system, six structure parameters for small and large bubble classes (their respective diameters d_{S}, d_{L}, volume fraction

f_S, f_L, and superficial gas velocities (U_{gS}, U_{gL}) can be obtained by solving the nonlinear optimization problem. This implies that these structure parameters not only obey the mass and momentum conservative equations but are governed by the stability condition reflecting the compromise between different dominant mechanisms.

The DBS model calculation on structure parameters and total gas holdup shows that the system structure evolves gradually with the increase of global superficial gas velocities, and then a jump change of gas holdup occurs, which coincidently corresponds to the transition from homogeneous and transition regimes to fully developed heterogeneous regime found in experiments (Camarasa *et al.*, 1999; Ruthiya *et al.*, 2005; Zahradnik *et al.*, 1997), as shown in Figure 17a. The prediction reflects some intrinsic evolution of the system structure whereas

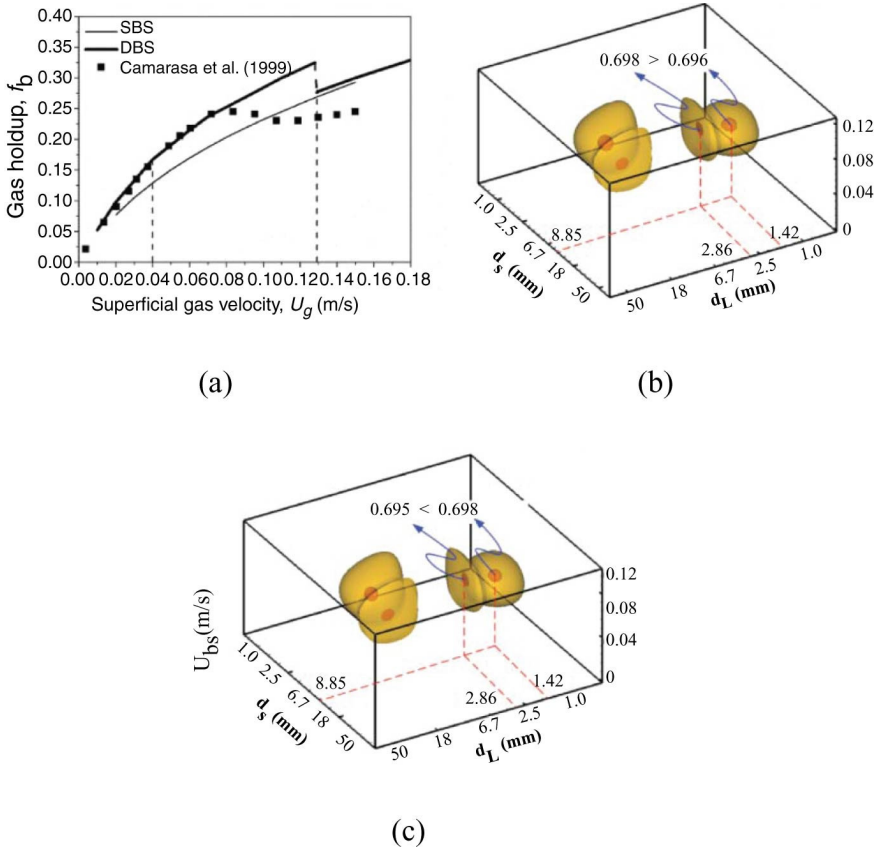

Figure 17 Physical explanation of regime transition in bubble columns (Yang *et al.*, 2007, 2010).

experiments in reality have to be influenced by extrinsic factors like aeration non uniformity generated from different distributors, liquid properties, and column geometries. A physical understanding on such regime transition can be obtained by scrutinizing Figure 17b and c. The global minimum of micro-scale energy dissipation falls into the right potential trough for 0.128 m/s of superficial gas velocity. However, it jumps into the left potential trough when U_g increases to 0.129 m/s. This jump change actually leads to the jump change of the diameter of small bubble class (see the dash lines. Note that the subscript S and L here only have symbolic significance and d_L stands for the small bubble class since the solutions are fully symmetrical to the cross-section plane of the cube) and hence other structure variables, implying that it is the stability condition which drives the evolution of system structure and finally leads to the regime transition.

Recognizing the role of stability condition in reflecting the compromise between dominant mechanisms and driving the evolution of multi-scale structure as an additional constraint besides mass and momentum conservative equations, direct coupling of the stability condition with CFD simulation should supply an ideal framework to theoretically simulate the gas–liquid flow. As a first approximation, we recently propose a simplified method to realize this coupling, just like that for modeling gas–solid flow in fluidization. The CFD simulation indicates that DBS-based model could obtain quite reasonable prediction with experiments for radial gas holdup, total gas holdup, and two-phase flow field as well as the regime transition in bubble columns without the need of adjusting any model parameters. Although this work need further validation and verification, the simulation has shown the great potential and advantage in modeling the complicated multi-scale structure and achieving a more intrinsic understanding of gas–liquid two-phase flow. For details, the interested readers are referred to our previous and upcoming publications (Chen *et al*., 2009a, 2009b; Yang *et al*., 2007, 2010, 2011).

In fact, extremum tendencies expressing the dominant mechanisms in systems like turbulent pipe flow (Li *et al*., 1999), gas–liquid–solid flow (Liu *et al*., 2001), granular flow, emulsions, foam drainages, and multiphase micro-/nanoflows also follow similar scenarios of compromising as in gas–solid and gas–liquid systems (Ge *et al*., 2007), and therefore, stability conditions established on this basis also lead to reasonable descriptions of the meso-scale structures in these systems. We believe that such an EMMS-based methodology accords with the structure of the problems being solved, and hence realize the similarity of the structures between the physical model and the problems. That is the fundamental reason why the EMMS-based multi-scale CFD improves the

conventional simulation methods for the corresponding systems. The effectiveness of the EMMS-based multi-scale CFD has been also indicated recently in the literature (Benyahia, 2010; Chalermsinsuwan *et al*., 2009; Hartge *et al*., 2009; Hou and Li, 2010; Jiradilok *et al*., 2006; Nikolopoulos *et al*., 2010a, 2010b; Qi *et al*., 2007; Wang *et al*., 2010a; Yang *et al*., 2009), and in the mean while, industrial applications of it help us continuously elaborate the multi-scale CFD approach.

4. INDUSTRIAL APPLICATIONS

In this section we will present some examples of using the EMMS-based multi-scale CFD to solve industrial problems, including fluid catalytic cracking (FCC) and CFB combustion.

4.1 Fluid catalytic cracking

Fluid catalytic cracking has been widely applied in petroleum refinery to convert crude oil into a variety of light products, including about 45% of gasoline worldwide (Chen, 2006). Direct products from FCC process normally contain too much olefin that is harmful to environments. To reduce the olefin content for cleaner fuels, the Research Institute of Petroleum Processing (RIPP), SINOPEC has developed a novel FCC process for maximizing *iso*-paraffins (MIP) (Xu *et al*., 2001). Besides catalyst, this new FCC process has a different design of reactor. The classical FCC reactor was altered by inserting an enlarged section in the middle of the riser, to favor the olefins transformation into *iso*-paraffins and aromatics through alkene isomerization and hydrogen transfer reactions.

Changing the mature FCC to novel design in commercial plants is challenging. Traditional method from lab test to industry step by step is rather time-consuming and costly, while numerical simulation could help boost this procedure provided with reliable model of hydrodynamics. In view of that, RIPP and Institute of Process Engineering (IPE) of Chinese Academy of Sciences (CAS) reached an agreement in 2001 to collaborate on hydrodynamics prediction by using EMMS model. At the time of that first cooperation, the best computing resource available to IPE was not powerful enough to allow a transient CFD simulation of the whole riser. Therefore, a steady-state EMMS model was used with extension to account for the axial distribution. The simulation was performed to predict the catalyst particles distribution. The results submitted to SINOPEC finally have helped the designer figure out the key parameters for the first set of novel FCC process installed in Gaoqiao, Shanghai in 2002, with capability of annual process of 1.4 million ton of crude oil.

Along with the successful running of this first demonstration plant, the MIP processes spread all over China through modifying existent FCC processes. Unlike building a reactor from scratch, modification is constrained by the old design. That results in various geometric factors in different MIP reactors, and hence, more complicated flow behaviors have been found during operation. To help implement the modification, it is necessary to determine the detailed flow behavior inside. As a result, a second collaboration between IPE and RIPP was started in 2005, to evaluate the flow behavior under various designs of inlet, outlet, and distributor as well as solids flux of catalyst particles. To this end, the simplified version of the EMMS-based multi-scale CFD has been used to predict the multiphase flow behavior (Lu *et al.*, 2007).

First, for validation, a series of experiments were performed on a cold-model rig of MIP reactor. Figure 18 shows snapshots of simulated solids distribution in the riser and the axial profile of cross-sectionally averaged voidage against experimental data. The clustering phenomenon that was found in experiments can be captured, and the predicted profile was in good agreement with the experimental data (Lu *et al.*, 2007). By comparison, CFD simulation without drag correction predicted a rather dilute riser without obvious clustering, which is contrary to experimental findings. On that basis, a series of 2D simulation of an

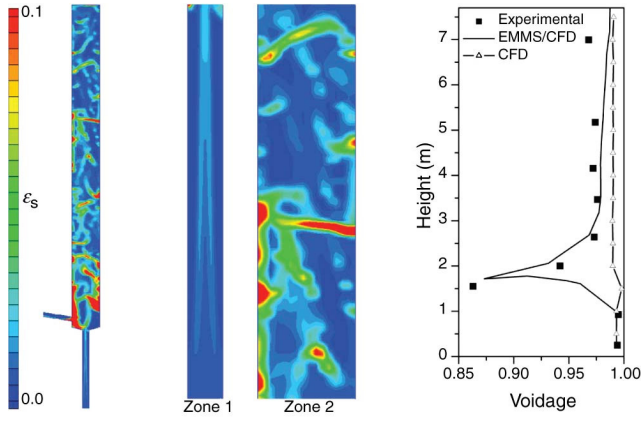

Figure 18 (a) Instantaneous plot of solids volume fraction in a laboratory-scale cold model of MIP reactor. (b) Sectioned snapshots of solids volume fraction in the first and second reaction zones. (c) Time-averaged axial profiles of voidage (—EMMS/CFD: 2D result with EMMS-based drag correlation; $-\Delta-$CFD: result with hybrid drag coefficient of Wen and Yu model and Ergun equation) (Lu *et al.*, 2007).

industrial MIP riser was performed. About 18,000 unstructured grids were generated to model the enlarged section of the riser as well as its inlet and outlet tube. It normally takes about 1 month for one typical case on a computer with one AMD246 CPU. A typical snapshot of the predicted solids distribution in the reactor is shown in Figure 19.

The most important information generated from this second collaboration is that the ''choking'' behavior was found in the MIP riser. As shown in Figure 20, we found the choking may occur in the second reaction zone under certain set of operating conditions. The understanding of that is critical to the design and operation as the industry needs that information to avoid the choking instability. However, as discussed in the above sections, the choking mechanism and even its phenomenon have caused hot disputes in the past decades. One reason is that we are still short of physics-based explanation. Another reason is that the choking was found dependent heavily on the riser height and geometric limitations, while it is quite difficult, if not impossible, for experimental researchers to carry out studies covering all those geometric factors and to unify the findings obtained from different

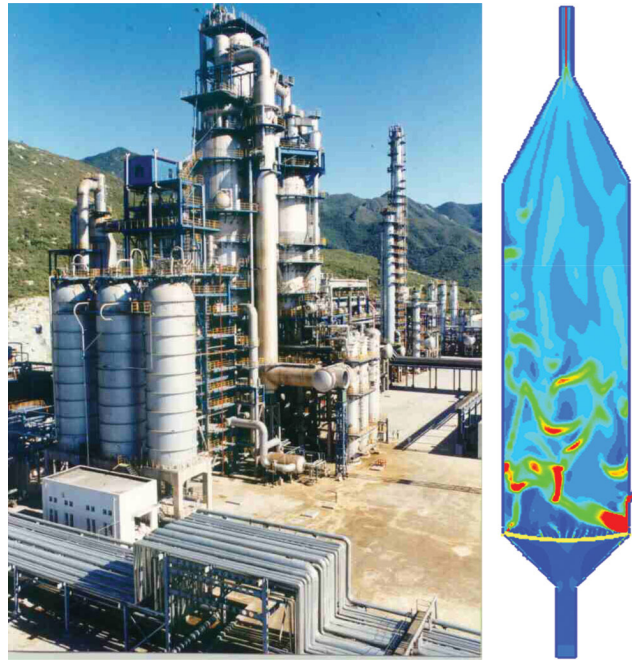

Figure 19 An industrial MIP reactor and the relevant simulation results of solids distribution.

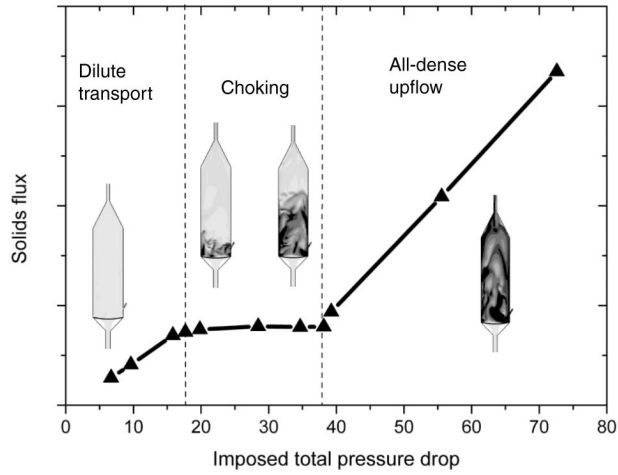

Figure 20 Predicted flow regime diagram of the industrial MIP reactor, with solids flux as a function of the imposed total pressure drop at fixed gas flow rate. The snapshots of voidage profile refer to the transition, from left to right, the dilute transport, choking transition in between with different solids inventory, to the dense fluidization (Lu *et al*., 2007).

research groups. By comparison, CFD simulations with reliable meso-scale modeling can be expected to help troubleshoot and tackle such hard problems readily.

The collaboration is still going on. The full-loop, 3D simulations of MIP reactors are being performed to help further scale-up. To some extent, the multi-scale CFD is beginning to take the place of virtual experiment for solving industrial problems, and it is emerging as a paradigm beneficial to both industry and academia.

4.2 CFB boiler

CFB with internal combustion can be traced back to the invention of aluminum hydroxide calcination technology by Lurgi (Reh, 1995). A typical CFB combustor mainly consists of a highly expanded fluidized bed furnace (riser), with solids externally circulated, through gas–solid cyclones or separators, standpipes, aerated siphons/valves, and, in some cases, external heat exchangers. CFB combustors have been applied widely together with gradual scale-up, from the first coal combustor of 84 MWth at Vereinigte Aluminium Werke AG (VAW) in Lünen to atmospheric utility boilers of 300 MWe installed in recent years and up to 800 MWe ultrasupercritical CFB boilers in project.

Scale-up and optimal design of CFB boilers require comprehensive knowledge on gas–solids two-phase flow and mixing, interphase heat/mass transfer, reaction, bed-to-wall heat extraction, and separation efficiency. These issues are strongly related with specific designs of coal particles and complex geometries under wide range of operating conditions, while measurements under high temperature over large-scale facilities are very hard to carry out. In this situation, CFD simulation is a good complement or alternative to facilitate design and operation. In literature, most of CFD simulations reported are limited to the furnace chamber and usually with 2D simplifications. However, as we have shown in simulating the ETH cold model CFB (Zhang *et al*., 2008), to better understand the manifold factors affecting CFB boilers, we need detailed information concerning, for example, the dynamic mixing of gas and solid fuels in each direction, the effects of various coal-feed inlets, solid-return valves, air-injection nozzles, and the pressure distribution around the whole loop, and so on. All these entail 3D, full-loop CFD simulations with reasonable models.

As discussed in the above sections, EMMS-based multi-scale CFD allows using very coarse-grid that is larger than in conventional CFD methods by 1–2 orders of magnitude without losing accuracy. That means it even enables reducing the computing load by 3–6 orders of magnitude. Such a merit is extremely useful to simulate a large CFB boiler, or else, a reasonable computation with billions of numerical grids may last for years and is unaffordable.

In what follows we will give an example of using the EMMS-based multi-scale CFD to study the complex hydrodynamics and reactions in an industrial 150 MWe CFB boiler, which was designed by Harbin Boiler Co. Ltd. and installed in Guangdong, China. The hydrodynamics part has been reported (Wang and Li, 2010; Zhang *et al*., 2010) and the reactive part is referred to more recent work of Zhang (2010).

As shown in Figure 21, the boiler consists of a furnace ($15.32 \times 7.22\,m^2$ in cross section and 36.5 m in height), two adiabatic cyclones, diplegs, and U-type loop-seal valves. The diameter of the two cyclones is 8.08 m; each dipleg is connected via two loop seals to the furnace. The primary air was assumed uniformly blown into the bottom of the furnace, and 26 secondary air and 2 slag-cooler inlets were all meshed according to the real design with uniform inflow. The gas flow rates at different inlets were set according to the designed values. An atmospheric pressure boundary was prescribed at the cyclone outlets. To save the computation cost, monodisperse particle with average diameter of 0.2 mm and density of $2000\,kg/m^3$ was assumed based on empirical data. At the walls, the nonslip boundary condition was used for the gas phase and a partial-slip boundary condition was used for the

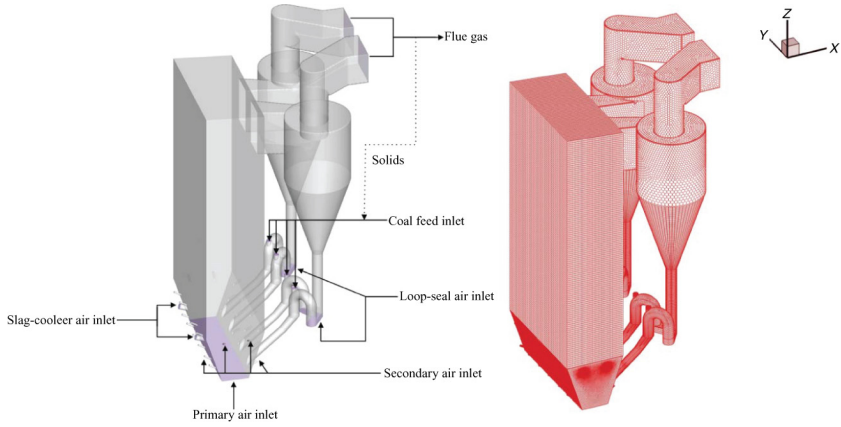

solid phase. For hydrodynamic simulations, the flow is assumed unaffected by reactions and the whole loop in Figure 21 was modeled under the design temperature of 917 °C. As the reaction was not explicitly introduced, to keep a constant solids inventory of the whole boiler, the solids entrained out of the cyclone outlets were returned to the furnace via the coal feed inlets. Fluent 6.3.26 was used as the solver with the drag coefficient modified by EMMS. As to the meshes, the boiler was divided into several blocks, where the connections between air inlets and the furnace were meshed with polyhedron, and the others were meshed with hexahedron, all with size scale of 0.1 m. In such a way, the total mesh number amounts to about 500,000. The turnaround time of such a simulation was about several weeks on a cluster of 2.6 GHz computers. More detailed description is referred to Zhang *et al*. (2010).

Figure 22 shows a snapshot of the solids distribution at the walls of the whole boiler. Below the secondary air inlets, clearly a dense bottom was formed. Above that, the dilute top region was predicted with various forms of clusters, most of which flow down along the wall as shown by the vector slice at the side wall. At the loop-seal valves, dense bottom regions were formed with bubbles. The solids captured by the cyclone were also in forms of certain kind of dynamic aggregates, falling down spirally along the wall. Unfortunately there is no data we can use to verify such complex phenomena. Obviously more efforts are needed to measure the flow behavior in such a hot facility.

A qualitative verification of this hot-model hydrodynamics relates with a seesaw phenomenon. For this phenomenon, Grace *et al*. have

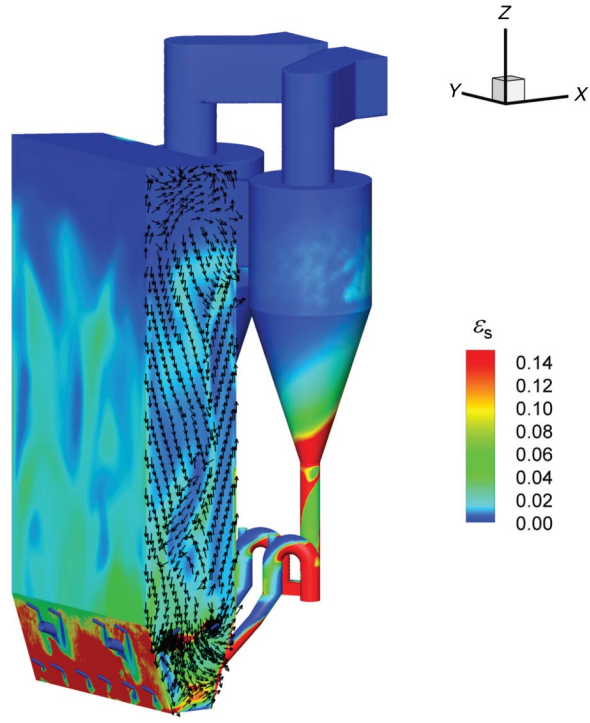

Figure 22 Snapshot of the solids distribution at all the walls together with a slice of the solids velocity vectors at the side wall.

addressed that, ''when two-phase suspensions are conveyed through identical parallel flow paths, the flow distribution can be significantly nonuniform in practice,'' and there is also maldistribution of gas–solids flow through identical parallel cyclones in their experiments (Grace *et al*., 2007; Masnadi *et al*., 2010). Figure 23 shows the simulated solid fluxes at the inlets of the two cyclones. During the monitored period of time, the averaged solid fluxes manifest no obvious difference as these two cyclones were designed and operated identically. However, their instant fluxes show the seesaw phenomenon—the maximum and minimum values of the fluxes alternates as to time, one minimum corresponding to another maximum. This can also be validated by the alternate appearance of dense aggregates near the cyclone inlets, as indicated by the circles in Figure 24. Such predicted phenomenon agrees well with the experimental results of Grace's group (Grace *et al*., 2007; Masnadi *et al*., 2010).

The reactive modeling was only performed for the furnace chamber limited to computing cost. Still a monodisperse solid phase was

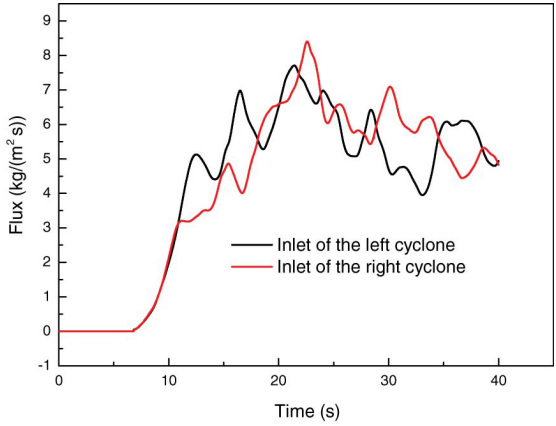

Figure 23 The seesaw phenomenon of area-averaged solid fluxes at the cyclone inlets (Zhang *et al*., 2010), in accordance with the experimental findings in identical parallel cyclones (Masnadi *et al*., 2010).

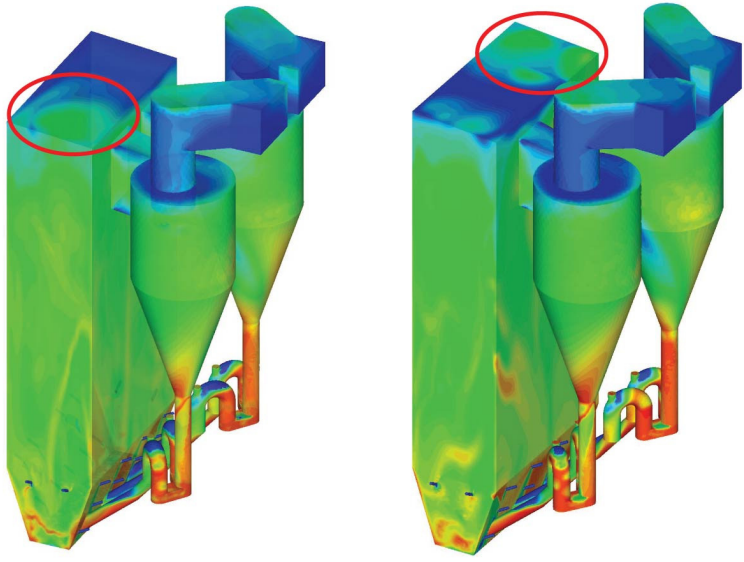

Figure 24 The seesaw phenomenon by instantaneous solids distribution in the boiler at simulation time of (a) No. 28.9 s and (b): No. 38.7 s. The red circles indicate high solids volume fraction on the top wall of the furnace (Zhang *et al*., 2010).

assumed, consisting of ash and carbon. The gas mixture was assumed to contain only N_2, O_2, and CO_2 to reduce the computation, while the heat effect of the other components such as the volatile and the moisture were considered only in the energy conservation equations. The EMMS/mass model was used to reframe the scalar conservation equations for mass fractions of carbon, O_2, and CO_2. The EMMS/matrix model was used to modify the drag coefficient. The bed-to-wall heat transfer has great effects on the convergence of code, for simplicity, constant temperatures at the walls were assumed. More detailed description should be referred to Zhang (2010) and Wang and Li (2010).

In all, the coal combustion is a very complex process and is far from being understood comprehensively. As a tentative solution to it, the EMMS-based multi-scale CFD allows using coarse-grid to predict its gas–solid flows without losing accuracy, and the multi-scale behavior of mass/heat transfer can be also integrated into this framework naturally. The current example has shown us the possibility and advantages of using this multi-scale CFD in dealing with large-scale CFB reactors with complex coupling of flow, transfers and reactions, though still preliminarily. More applications of such an approach can be expected to bring us a new paradigm for reactive multiphase flow simulations.

5. SUMMARY

Meso-scale structure is the bridge between micro-scale nature and macro-scale performance, and hence it is critical to characterize complex systems in chemical engineering. Without meso-scale modeling, the conventional TFM fails to describe the intrinsic structural effects and characteristic behavior of fluidized beds. In contrast, based on EMMS modeling, the multi-scale CFD approach features intrinsic resolution of meso-scale structures and enables almost grid-independent solution of the gas–solid two-phase flows. Such a variational type of multi-scale CFD has been used to simulate various CFB reactors, including industrial applications in FCC, CFB boiler, and so on. It has proved to improve both computational efficiency and accuracy significantly, in the sense that it allows using much coarser grid without losing accuracy, succeeds in predicting the circulating solids flux, revealing the mechanisms of the choking phenomena, resolving the disputes in transport phenomena of gas-fluidized beds, and so on. All these suggest a breakthrough in CFD simulation can be achieved by resolving the structure of the physical model in accordance with that of the problems being solved. With that methodology in mind, we are expected to

unfold a new paradigm for the simulation of multiphase flows and reactors.

NOMENCLATURE

a	the inert term or acceleration of particles, m/s^2
Ar	Archimedes number
C_D	effective drag coefficient for a particle
d_c	cluster diameter, m
d_L	bubble diameter of large bubbles, m
d_p	particle diameter, m
d_S	bubble diameter of small bubbles, m
D_m	molecular diffusion, m^2/s
f	volume fraction of clusters
f_L	volume fraction of large bubbles
f_S	volume fraction of small bubbles
g	vector of gravity acceleration, m/s^2
G_s	solids flux, kg/(m^2 s)
h	heat transfer coefficient, W/(m^2 K)
H	riser height, m
H_0	initial bed height, m
H_D	heterogeneity index
k	mass transfer coefficient between gas and particle, m/s
k_p	mass transfer coefficient between gas and particle, m/s
k_r	ozone decomposition rate, 1/s
N_{break}	rate of energy consumption due to bubble breakage and coalescence per unit mass, m^2/s^3
N_{st}	mass-specific energy consumption for suspending and transporting particles, W/kg
N_{surf}	rate of energy dissipation due to bubble oscillation per unit mass, m^2/s^3
N_{turb}	rate of energy dissipation in turbulent liquid phase per unit mass, m^2/s^3
Re	Reynolds number
Re_p	local superficial Reynolds number ($\rho_g d_p U_s/_g$)
Re_0	global superficial Reynolds number ($\rho_g d_p U_g/_g$)
Sc	Schmidt number ($_g/\rho_g D_m$)
Sh	Sherwood number (kd_p/D_m)
u	real velocity, m/s
U	superficial velocity, m/s

W_{st}	volume-specific energy consumption for suspending and transporting particles, W/m^3
Y	mass fraction of gas species

Greek letters

α_p	outer surface area per volume of particles, m^2/m^3
β	drag coefficient with structure in a control volume, $kg/(m^3\,s)$
β_0	drag coefficient without structure in a control volume, $kg/(m^3\,s)$
ε	time-averaged voidage
ε_g	voidage
ε_{max}	maximum voidage for particle aggregation
ε_{mf}	minimum fluidization voidage
ε_s	solids concentration
ε_{s0}	averaged solids concentration
	viscosity, Pa s
ρ	density, kg/m^3
Γ	interphase mass exchange rate, $kg/(m^3\,s)$

Subscripts

A	component A
c	dense phase
f	dilute phase
g	gas phase
gc	gas phase in the dense phase
gf	gas phase in the dilute phase
i	meso-scale interphase
imp	imposed pressure across the riser
L	large bubbles
mf	minimum fluidization
ovr	averaging over bed height
p	particle
pc	solid phase in the dense phase
pf	solid phase in the dilute phase
s	slip velocity
S	small bubbles
sat	saturation
sc	slip in the dense phase
sf	slip in the dilute phase
si	slip at the meso-scale interphase

T terminal velocity
y carrier gas phase

(Bold characters are for vectors or tensors.)

ACKNOWLEDGMENTS

The authors acknowledge the financial supports provided by the National Natural Sciences Foundation of China (NSFC) under the Grant No. 20821092, Ministry of Science and Technology (MOST) of China under the Grant No. 2008BAF33B01, and Chinese Academy of Sciences (CAS) under the Grant No. KGCX2-YW-222.

REFERENCES

Agrawal, K., Loezos, P. N., Syamlal, M. and Sundaresan, S., *J. Fluid Mech.* **445**, 151–185 (2001).
Andrews, A. T., Loezos, P. N. and Sundaresan, S., *Ind. Eng. Chem. Res.* **44**(16), 6022–6037 (2005).
Andrews, M. J. and O'Rourke, P. J., *Int. J. Multiphase Flow* **22**(2), 379–402 (1996).
Basu, P. and Fraser, S. A., ''Circulating Fluidized Bed Boilers: Design and Operations''. Butterworth-Heinemann, Boston (1991).
Benyahia, S., *Ind. Eng. Chem. Res.* **49**(11), 5122–5131 (2010).
Bi, H. T., Grace, J. R. and Zhu, J., *Int. J. Multiphase Flow* **19**(6), 1077–1092 (1993).
Bird, R. B., Stewart, E. and Lightfoot, E. N., ''Transport Phenomena''. Wiley, New York (1960).
Breault, R. W., *Powder Technol.* **163**(1–2), 9–17 (2006).
Camarasa, E., Vial, C., Poncin, S., Wild, G., Midoux, N. and Bouillard, J., *Chem. Eng. Proc.* **38**, 329–344 (1999).
Chalermsinsuwan, B., Piumsomboon, P. and Gidaspow, D., *Chem. Eng. Sci.* **64**, 1212–1222 (2009).
Chen, Y., *Powder Technol.* **163**, 2–8 (2006).
Chen, F. and Ge, W., *Particuology* **8**(4), 332–342 (2010).
Chen, F., Ge, W., Guo, L., He, X., Li, B., Li, J., *Particuology* **7**, 332–335 (2009).
Chen, F., Ge, W., Wang, L. and Li, J., *Microfluidics Nanofludics* **5**(5), 639–653 (2008).
Chen, J., Yang, N., Ge, W. and Li, J., *Ind. Eng. Chem. Res.* **48**, 290–301 (2009).
Chen, J., Yang, N., Ge, W. and Li, J., *Ind. Eng. Chem. Res.* **48**, 8172–8179 (2009).
Crowe, C. T., ''Multiphase Flow Handbook''. CRC Press, Boca Raton (2006).
De Wilde, J., *Phys. Fluids* **17**, 113304 (2005).
Dixon, A. G., Nijemeisland, M. and Hugh Stitt, E., Packed tubular reactor modeling and catalyst design using computational fluid dynamics, in ''Advances in Chemical Engineering'', **Vol. 31**, pp. 307–389, Elsevier, Amsterdam (2006).
Dong, W., Wang, W. and Li, J., *Chem. Eng. Sci.* **63**, 2798–2810 (2008).
Dong, W., Wang, W. and Li, J., *Chem. Eng. Sci.* **63**, 2811–2823 (2008).
Dry, R. J., Christensen, I. N. and White, C. C., *Powder Technol.* **52**, 243 (1987).
Dry, R. J. and White, C. C., *Powder Technol.* **70**, 277 (1992).

Dudukovic, M. P., *Science* **325**, 698–701 (2009).
Ergun, S., *Chem. Eng. Prog.* **48**, 89–94 (1952).
Ferziger, J. H., Subgrid-scale modeling, *in* ''Large Eddy Simulation of Complex Engineering and Geophysical Flows'' (B. Galperin, S. A. Orszag, Eds.), pp. 37–54. Cambridge University Press, Cambridge (1993).
Gage, D. H., Schiffer, M., Kline, S. J. and Reynolds, W. C., The non-existence of a general thermodynamic variational principle, *in* ''Non-Equilibrium Thermodynamics, Variational Techniques and Stability'' (R. J. Donnelly, R. Herman, I. Prigogine, Eds.), p. 286. University of Chicago Press, Chicago (1966).
Ge, W. and Chen, F., et al., ''GPU-Based Multi-Scale Discrete Simulations and Parallel Computation''. Science Press, Beijing (2009) (in Chinese).
Ge, W., Chen, F. and Gao, J., et al., *Chem. Eng. Sci.* **62**(13), 3346–3377 (2007).
Ge, W. and Li, J., Pseudo-particle approach to hydrodynamics of gas/solid two-phase flow, *in* ''Circulating Fluidized Bed Technology V'' (J. Li, M. Kwauk, Eds.), pp. 260–265. Science Press, Beijing (1996).
Ge, W. and Li, J., *Chem. Eng. Sci.* **57**, 3993–4004 (2002).
Ge, W. and Li, J., *Chem. Eng. Sci* **58**(8), 1565–1585 (2003).
Ge, W., Wang, W., Dong, W., Wang, J., Lu, B., Xiong, Q. and Li, J., Multi-scale structure—a challenge of CFD for CFBs, *in* ''Proceedings of the 9th International Conference of Circulating Fluidized Bed'' (J. Werther, E. U. Hartge, Eds.), May 13–16, Hamburg.
Geldart, D., *Powder Technol.* **7**, 185–195 (1973).
Gidaspow, D., ''Multiphase Flow and Fluidization: Continuum and Kinetic Theory Descriptions''. Academic Press, Boston (1994).
Goldhirsch, I., *Ann. Rev. Fluid Mech.* **35**, 267–293 (2003).
Grace, J. R., Influence of riser geometry on particle and fluid dynamics in circulating fluidized beds risers, *in* ''Proceedings of the 5th International Conference of Circulating Fluidized Bed'' (M. Kwauk, J. Li, Eds.), May 28–31, Beijing.
Grace, J. R., Cui, H. and Elnashaie, S. S., *Can. J. Chem. Eng.* **85**(5), 662–668 (2007).
Gunn, D. J., *Int. J. Heat Mass Transfer* **21**, 467–476 (1978).
Harris, A. T., Davidson, J. F. and Thorpe, R. B., *Powder Technol.* **127**, 128–143 (2002).
Hartge, E. -U., Ratschow, L., Wischnewski, R. and Werther, J., *Particuology* **7**(4), 283–296 (2009).
Herbert, P., Reh, L. and Nicolai, R., *AIChE Symp. Ser.* **321**, 95 (1999) 61–66.
Hou, C. and Ge, W., *Chem. Eng. Sci.* **62**, 6794–6805 (2007).
Hou, B. and Li, H., *Chem. Eng. J.* **157**(2–3), 509–519 (2010).
Hu, N., Zhang, H., Yang, H., Yang, S., Yue, G., Lu, J. and Liu, Q., *Powder Technol.* **196**(1), 8–13 (2009).
Igci, Y., Andrews, A. T., Sundaresan, S., Pannala, S. and O'Brien, T., *AIChE J.* **54**, 1431–1448 (2008).
Jin, G., He, G. and Wang, L., *Phys. Fluids* **22**(5) 055106.
Jiradilok, V., Gidaspow, D., Damronglerd, S., Koves, W. J. and Mostofi, R., *Chem. Eng. Sci.* **61**(17), 5544–5559 (2006).
Kettenring, K. N. and Manderfield, E. L., *Chem. Eng. Prog.* **46**(3), 139–145 (1950).
Kunii, D. and Levenspiel, O., ''Fluidization Engineering, 2nd ed. Butterworth-Heinemann, Boston (1991).
Levenspiel, O., ''Chemical Reaction Engineering'', 3rd ed. John Wiley & Sons, New York (1999).
Li, J., Multi-Scale Modeling and Method of Energy Minimization for Particle–Fluid Two Phase Flow, Ph.D. thesis (in Chinese), Institute of Chemical Metallurgy, Chinese Academy of Sciences, Beijing (1987).

Li, J., Chen, A., Yan, Z., Xu, G. and Zhang, X., Particle-fluid contacting in circulating fluidized beds, *in* ''Preprint Volume for Circulating Fluidized Beds IV'' (A. A. Avidan, Ed.), pp. 49–54. AIChE, Somerset (1993).
Li, J. and Ge, W., *Chem. Eng. Sci.* **62**, 3285–3286 (2007).
Li, J., Ge, W. and Kwauk, M., arXiv:0912.5407v3 (2009).
Li, J., Ge, W., Zhang, J., Gao, S., Wang, W., Yang, N., Sun, Q., Gao, J. (2007). Analytical multi-scale methodology for fluidization systems—retrospect and prospect. In: Berruti, F., Bi, X., Pugsley, T. (eds.), The 12th International Conference on Fluidization, Vancouver, Canada.
Li, J., Ouyang, J., Gao, S., Ge, W., Yang, N. and Song, W., ''Multiscale Simulation of Particle-Fluid Complex Systems (in Chinese)''. Science Press, Beijing (2005).
Li, J. and Kwauk, M., ''Particle-Fluid Two-Phase Flow—the Energy-Minimization Multi-Scale Method''. Metallurgical Industry Press, Beijing (1994).
Li, J. and Kwauk, M., *Ind. Eng. Chem. Res.* **40**, 4227–4237 (2001).
Li, J. and Kwauk, M., *Chem. Eng. Sci.* **58**, 521–535 (2003).
Li, J., Zhang, J., Ge, W. and Liu, X., *Chem. Eng. Sci.* **59**, 1687–1700 (2004).
Li, J., Zhang, Z., Ge, W., Sun, Q. and Yuan, J., *Chem. Eng. Sci.* **54**(8), 1151–1154 (1999).
Lin, Q., Wei, F. and Jin, Y., *Chem. Eng. Sci.* **56**(6), 2179–2189 (2001).
Liu, X., Gao, S. and Li, J., *Chem. Eng. J.* **108**(3), 193–202 (2005).
Liu, Y., Ge, W., Wang, J., Chen, J., Yang, N., Wang, W. and Li, J. *Powder Technol*. (2010) (accepted).
Liu, M., Li, J. and Kwauk, M., *Chem. Eng. Sci.* **56**, 6805–6812 (2001).
Lu, B., EMMS-based Meso-Scale Model and Its Application in Simulating Gas-Solid Two-Phase Flows, Ph.D. thesis (in Chinese), Institute of Process Engineering, Chinese Academy of Sciences, Beijing (2009).
Lu, B., Wang, W. and Li, J., et al., *Chem. Eng. Sci.* **62**, 5487–5494 (2007).
Lu, B., Wang, W. and Li, J., *Chem. Eng. Sci.* **64**, 3437–3447 (2009).
Lu, B., Wang, W. and Li, J. *Chem. Eng. Sci.* (2011) (in revision).
Ma, J., Ge, W., Wang, X., Wang, J. and Li, J., *Chem. Eng. Sci.* **61**, 7096–7106 (2006).
Ma, J., Ge, W., Xiong, Q., Wang, J. and Li, J., *Chem. Eng. Sci.* **64**, 43–51 (2009).
Manyele, S. V., Parssinen, J. H. and Zhu, J. -X., *Chem. Eng. J.* **88**, 151–161 (2002).
Masnadi, M. S., Grace, J. R., Elyasi, S. and Bi, X., *Sep. Purif. Technol*. **72**(1), 48–55 (2010).
Matsen, J. M., *Powder Technol*. **32**, 21–33 (1982).
Meng, F., Wang, W. and Li, J., A method of measuring velocity and acceleration of particle clusters in two-phase flows. Chinese Patent No. 200910082721.0 (2009).
Monaghan, J. J., *Rep. Prog. Phys.* **68**, 1703–1759 (2005).
Monaghan, J. J. and Kocharyan, A., *Comp. Phys. Commun.* **87**(1–2), 225–235 (1995).
Nikolopoulos, A., Atsonios, K., Nikolopoulos, N., Grammelis, P. and Kakaras, E., *Chem. Eng. Sci.* **65**(13), 4089–4099 (2010).
Nikolopoulos, A., Papafotiou, D., Nikolopoulos, N., Grammelis, P. and Kakaras, E., *Chem. Eng. Sci.* **65**(13), 4080–4088 (2010).
Niksa, S., Liu, G. and Hurt, R. H., *Prog. Energy Combust. Sci.* **29**, 425–477 (2003).
Ouyang, S., Li, X. -G. and Potter, O. E., *AIChE J.* **41**(6), 1534–1542 (1995).
Pope, S. B., ''Turbulent Flows''. Cambridge University Press, Cambridge (2000).
Prigogine, I., ''Introduction to Thermodynamics of Irreversible Processes''. Wiley Interscience, New York (1967).
Qi, H., Li, F., Xi, B. and You, C., *Chem. Eng. Sci.* **62**, 1670–1681 (2007).
Ranz, W. E., *Chem. Eng. Prog.* **48**(5), 247–253 (1952).
Reh, L., Fluid dynamics of CFB combustors, *in* ''Proceedings of the 5th International Conference on Circulating Fluidized Beds'' (M. Kwauk, J. Li, Eds.), pp. 1–15. Beijing (1996).

Reh, L. and Li, J., Measurement of voidage in fluidized beds by optical probe, *in* ''Circulating Fluidized Beds Technology III'' (P. Basu, M. Horio, M. Hasatani, Eds.), p. 105. Pergamon Press, Oxford, UK (1991).

Resnick, W. and White, R. R., *AIChE J.* **45**(6), 377–390 (1949).

Ruthiya, K. C., Chilekar, V. P., Warnier, M. J. F., van der Schaaf, J., Kuster, B. F. M., Schouten, J. C. and van Ommen, J. R., *AIChE J.* **51**, 1951–1965 (2005).

Sharma, A. K., Tuzla, K., Matsen, J. and Chen, J. C., *Powder Technol.* **111**, 114–122 (2000).

Soong, C. H., Tuzla, K. and Chen, J. C., Identification of particle clusters in circulating fluidized bed, A. A. Avidan, Ed.), pp. 615–620. **Vol. IV**, AIChE, New York (1994).

Subbarao, D. and Gambhir, S., Gas to particle mass transfer in risers, in ''Proceedings of 7th International Circulating Fluidized Beds Conference'', pp. 97–104, Canadian Society for Chemical Engineering, Niagara Falls.

Turns, S. R., ''An Introduction to Combustion: Concepts and Applications, 2nd ed. McGraw-Hill, Boston (2000).

Venderbosch, R. H., Prins, W. and van Swaaij, W. P. M., *Can. J. Chem. Eng.* **77**(2), 262–274 (1999).

Van der Ham, A. G. J., Prins, W. and Van Swaaij, W. P. M., Hydrodynamics and mass transfer in a regularly packed circulating fluidized bed, *in* ''Circulating Fluidized Bed Technology III'' (P. Basu, M. Horio, M. Hasatani, Eds.), p. 605. Pergamon Press, Oxford, UK (1991).

Van der Hoef, M. A., Ye, M., van sint Annaland, M., Andrews IV, A. T., Sundaresan, S. and Kuipers, J. A. M., Multiscale modeling of gas-fluidized beds, *in* ''Advances in Chemical Engineering'', Vol. 31, pp. 65–149. Academic Press, New York (2006).

Wang, L., Multi-Scale Mass Transfer Model and Experimental Validation for Heterogeneous Gas-Solid Two-Phase Flow, Ph.D. thesis (in Chinese), Chinese Academy of Science, Beijing (2002).

Wang, J., *Chem. Eng. Sci.* **63**(8), 2294–2298 (2008).

Wang, W. and Li, J., *Chem. Eng. Sci.* **62**, 208–231 (2007).

Wang, W. and Li, J., Modeling of circulating fluidized bed combustion, Chapter 12 (M. Lackner, F. Winter, A. K. Agarwal, Eds.), pp. 437–472. **Vol. 4**, Wiley-VCH, Berlin (2010).

Wang, X., Liao, L., Fan, B., Jiang, F., Xu, X., Wang, S. and Xiao, Y., *Fuel Process. Technol.* **91** (8), 927–933 (2010a).

Wang, W., Lu, B., Dong, W. and Li, J., *Can. J. Chem. Eng.* **86**, 448–457 (2008).

Wang, W., Lu, B. and Li, J., *Chem. Eng. Sci.* **62**, 814–819 (2007).

Wang, W., Lu, B., Zhang, N., Shi, Z. and Li, J., *Int. J. Multiphase Flow* **36**, 109–118 (2010b).

Wang, J., Van der Hoef, M. A. and Kuipers, J. A. M. *Chem. Eng. Sci.***64**(3), 622–625 (2009).

Wang, L., Yang, N. and Li, J., *Chem. Eng. Commun.* **192**, 1636–1654 (2005).

Wen, C. Y. and Yu, Y. H., *Chem. Eng. Symp. Ser.* **62**(62), 100–111 (1966).

Wolf-Gladrow, D. A., ''Lattice-Gas Cellular Automata and Lattice Boltzmann Models: An Introduction''. Springer-Verlag, Berlin (2000).

Xiong, Q., Li, B., Chen, F., Ma, J., Ge, W. and Li, J., *Chem. Eng. Sci.* **65**, 5356–5365 (2010).

Xu, J., Qi, H., Fang, X., Ge., W., Wang, X., Xu, M., Chen, F., He, X. and Li, J. Particuology (2010b) (accepted).

Xu, Y., Zhang, J. and Rong, J., *Petrol. Process. Petrochem.* **32**(8), 1–5 (2001) (in Chinese).

Yang, W., *Ind. Eng. Chem. Res.* **43**(18), 5496–5506 (2004).

Yang, N., Chen, J., Ge, W. and Li, J., *Chem. Eng. Sci.* **65**, 517–526 (2010).

Yang, N., Chen, J., Zhao, H., Ge, W. and Li, J., *Chem. Eng. Sci.* **62**, 6978–6991 (2007).

Yang, N., Wang, W., Ge, W. and Li, J., *Chem. Eng. J.* **96**, 71–80 (2003).

Yang, N., Wang, W., Ge, W. and Li, J., *Ind. Eng. Chem. Res.* **43**, 5548–5561 (2004).

Yang, N., Wu, Z., Chen, J., Wang, Y. and Li, J. *Chem. Eng. Sci.* (2011) (in press).

Yang, B., Zhou, X., Yang, X., Chen, C. and Wang, L., *AIChE J.* **55**(8), 2138–2149 (2009).

Yu, Z. Q. and Jin, Y., Heat and mass transfer, Academic Press, New York (1994).
Zahradnik, J., Fialova, M., Ruzicka, M., Drahos, J., Kastanek, F. and Thomas, N. H., *Chem. Eng. Sci.* **52**, 3811–3826 (1997).
Zhang, N., EMMS-based Meso-Scale Mass Transfer Model and Its Application to Circulating Fluidized Bed Combustion Simulation, Ph.D. thesis (in Chinese), Institute of Process Engineering, Chinese Academy of Sciences, Beijing (2010).
Zhang, J., Ge, W. and Li, J., *Chem. Eng. Sci.* **60**(11), 3091–3099 (2005).
Zhang, N., Lu, B., Wang, W. and Li, J., *Particuology* **6**, 529–539 (2008).
Zhang, N., Lu, B., Wang, W. and Li, J., *Chem. Eng. J.* **162**, 821–828 (2010).
Zhang, D. Z. and VanderHeyden, W. B., *Int. J. Multiphase Flow* **28**, 805–822 (2002).
Zhao, H., Multi-scale Modeling of Gas-Liquid (Slurry) Reactors, Ph.D. thesis (in Chinese), Institute of Process Engineering, Chinese Academy of Sciences, Beijing (2006).